
General OOD Detection via Model-aware and Subspace-aware Variable Priority

 Min Lu* .  Hemant Ishwaran *†

Out-of-distribution (OOD) detection is essential for determining when a supervised model encounters inputs that differ meaningfully from its training distribution. While widely studied in classification, OOD detection for regression and survival analysis remains limited due to the absence of discrete labels and the challenge of quantifying predictive uncertainty. We introduce a framework for OOD detection that is simultaneously model aware and subspace aware, and that embeds variable prioritization directly into the detection step. The method uses the fitted predictor to construct localized neighborhoods around each test case that emphasize the features driving the model’s learned relationship and downweight directions that are less relevant to prediction. It produces OOD scores without relying on global distance metrics or estimating the full feature density. The framework is applicable across outcome types, and in our implementation we use random forests, where the rule structure yields transparent neighborhoods and effective scoring. Experiments on synthetic and real data benchmarks designed to isolate functional shifts show consistent improvements over existing methods. We further demonstrate the approach in an esophageal cancer survival study, where distribution shifts related to lymphadenectomy identify patterns relevant to surgical guidelines.

Keywords

Out-of-distribution detection · Model-aware detection · Variable prioritization · Release regions · Subspace analysis

1. Introduction

Detecting when a predictive model encounters inputs that differ from those seen during training, commonly referred to as *out-of-distribution* (OOD) detection, is critical for maintaining the reliability of machine learning systems [1, 2]. Since OOD data are not available during training, the challenge is to identify such cases at test time using only information from the *in-distribution* (ID) data. This goal differs from that of anomaly detection, which typically targets statistical outliers or points lying in low-density regions of the feature space. OOD detection instead focuses on shifts in the data-generating process that can undermine the validity of a fitted model, even when individual inputs do not look like classical outliers.

Let (X, Y) denote a random pair with joint distribution \mathbb{P} , where $X \in \mathbb{R}^d$ represents the covariate vector and Y is the outcome of interest. Our focus is on supervised learning problems in which X is a structured collection of features, as encountered in regression and survival models widely used in clinical and scientific applications. In the machine learning literature this setting

*Division of Biostatistics, Miller School of Medicine, University of Miami, Miami, USA

†Corresponding Author

Min Lu (m.lu6@umiami.edu)

Hemant Ishwaran (hishwaran@med.miami.edu)

is sometimes described as tabular data, and the central aspect is that each component of X has an interpretable role and contributes in potentially different ways to the prediction task. This structure motivates a model-centered view of OOD behaviour.

Throughout, we use the term “anomaly” to describe a test input X^* for which the joint distribution $\mathbb{P}_{X,Y}^*$ differs from the training distribution $\mathbb{P}_{X,Y}$. Such differences can arise for many reasons, including shifts in patient populations, changes in measurement processes, or covariate patterns that were rarely or never observed during training. The key question, however, is not simply whether $\mathbb{P}_X^* \neq \mathbb{P}_X$, but whether this shift affects the predictive relationship the model has learned. That relationship is encoded in the conditional distribution $\mathbb{P}_{Y|X}$, which dictates how the model maps features to outcomes. We therefore regard an input as *functionally* OOD when $\mathbb{P}_{Y|X}^* \neq \mathbb{P}_{Y|X}$ over regions of the feature space that the model relies upon. On the other hand, shifts confined to nuisance or noise coordinates may alter the marginal distribution \mathbb{P}_X without changing $\mathbb{P}_{Y|X}$; such inputs can appear unusual under \mathbb{P}_X yet remain effectively ID from the model’s perspective [3]. This distinction emphasizes that OOD detection should prioritize changes that threaten predictive validity while discounting perturbations along irrelevant directions. It also clarifies why criteria based solely on low density in \mathbb{P}_X are not sufficient for ensuring model reliability and motivates approaches that explicitly assess whether a test input alters the model’s learned functional relationship.

1.1. Approach

Building on this principle, we consider a class of OOD methods that are *model aware*, meaning they capture how the fitted model maps inputs to outputs, and *subspace aware*, meaning they focus on the coordinates most relevant to prediction. These methods are particularly important in high dimensional settings, where meaningful changes in a small subset of features can be masked by variation in many irrelevant dimensions, leading to missed detections or false alarms.

Most existing approaches to OOD detection have been developed for classification problems, where discrete labels make it possible to compute confidence scores from class probabilities or related transformations. Far fewer methods address continuous output models, where confidence estimation is less direct and high dimensionality can amplify the masking effect of irrelevant features. As a result, detectors that operate globally on the full input space often struggle to separate variation that affects prediction from variation that does not.

To address these challenges, we propose a general-purpose OOD detection framework that embeds variable prioritization directly into the detection process. By constructing localized regions of feature space from the model’s learned structure and computing scores within these task-relevant subspaces, the framework prioritizes changes that threaten predictive validity and discounts irrelevant variation. This design makes the approach broadly applicable, including in regression and survival settings where traditional global methods often struggle.

1.2. Summary of Main Contributions

Our main contributions can be summarized as follows. (1) We formalize a model-aware, subspace-aware framework for OOD detection that directly incorporates variable prioritization into the scoring mechanism. (2) We develop a copula-based strategy for anomaly generation that provides controlled, flexible mechanisms for simulating OOD shifts in marginal behavior or joint dependence, enabling rigorous benchmarking. (3) We demonstrate the method’s applicability across outcome types and problem scales, including regression, survival analysis, large-scale public benchmarks, and a clinical case study on esophageal cancer, where distribution shifts related to lymphadenectomy are evaluated for their relevance to surgical guidelines. (4) To support transparency and reproducibility, we provide an open-source R package `varPro` available

at <https://github.com/kogalur/varPro>. Public benchmark datasets and microarray data used for experimentation are available from cited references.

1.3. Organization

The paper is organized as follows. Section 2 reviews related work and highlights the novel contributions of our approach. Section 3 details the proposed methodology, and Section 4 describes the comparison methods used for evaluation. Section 5 presents our extensive benchmarking results. Section 6 details our method’s application to a survival analysis of esophageal cancer. Section 7 concludes with a summary and discussion of limitations.

2. Related Work

Research on out-of-distribution (OOD) behaviour has grown rapidly in recent years, spanning anomaly detection, open-set recognition, selective prediction, domain generalization, and OOD detection [2, 4, 5, 6]. A series of recent survey articles organize the growing body of OOD work. These roughly break the area into methods designed for supervised learning [2, 4, 5] and those focusing on structured domains such as graphs and time series [7, 8, 9]. In this paper we focus on test-time OOD detection for supervised models, with an emphasis on regression and survival analysis and on detecting functionally OOD inputs that alter the conditional relationship $P_{Y|X}$ learned by the model.

2.1. Classification-based OOD Detection

Most OOD detection work targets classification tasks, where discrete labels provide natural confidence scores. Early methods such as Maximum Softmax Probability (MSP) [1] and ODIN’s temperature-scaled logit perturbations [10] determine OOD status based on transformed class probabilities, while energy-based scoring replaces softmax confidences with an un-normalized logit energy [11]. Mahalanobis-based methods instead measure the distance from a test feature to class-conditional centroids in a learned representation space [12].

More recent work refines these scores in several directions. Representation-based methods such as deep nearest neighbors [13] and posterior-sampling approaches [14] operate directly in learned feature space, while other techniques explicitly shape the in-distribution representation or its statistics to improve ID/OOD separation [15]. Complementary studies on feature sparsity [16] show that inducing sparse, low-redundancy activations can also enhance OOD detection performance. Subspace-based methods further decompose activations into decisive and residual components [17, 18], or apply kernel PCA and related spectral criteria [19]. These methods achieve impressive performance on image and text benchmarks, but they are tied to discrete labels and deep feature extractors, and their reliance on fixed global representations makes it less clear how to extend them to continuous outcomes or tabular clinical settings.

2.2. Regression, Survival, and Tabular OOD Detection

For models with continuous or time-to-event outcomes, OOD detection has largely followed an uncertainty-based paradigm. Deep ensembles [20] and Monte Carlo dropout [21] introduce stochasticity at inference time and flag inputs with high predictive variance as OOD. Evidential deep regression [22], prior networks [23], and predictor entropy methods for regression [24] learn explicit epistemic uncertainty distributions and use entropy as a detection signal. Gaussian processes and deep kernel learning [25, 26, 27] offer Bayesian variance estimates, and have been adapted for OOD detection in state-space models and medical imaging applications [28, 29]. In medical regression and digital pathology, [30] compare predictive uncertainty estimators for OOD detection in continuous tasks, and recent work in bioinformatics surveys OOD learning

challenges for high-dimensional omics data [31]. Despite these advances, most methods treat OOD detection as a *global* function of predictive uncertainty in the full feature space, making no attempt to distinguish perturbations along important versus nuisance directions.

Recent tabular and clinical studies emphasize the practical impact of OOD inputs on risk prediction and decision support. [32] propose an OOD reject option (ODROP) for disease onset prediction that trains a separate OOD detector on health-check data and rejects OOD cases before applying a tabular prediction model. [33] introduce a large benchmark for OOD detection in medical tabular data, highlighting over-confidence of standard models and the sensitivity of detectors to the type of shift. Broader reviews on OOD detection in medical imaging and electronic-health-record models reinforce the need for methods that are both accurate and interpretable in clinical settings [34, 35]. To our knowledge, however, there is little work on model and subspace-aware OOD detection in regression or survival models that explicitly leverages variable importance and predictive structure when defining OOD scores.

2.3. Geometry and Subspace Approaches

A complementary line of work adopts a geometric perspective, comparing test inputs to structural patterns in the training distribution. In classification, Mahalanobis distance in feature space [12] and Gaussian-mixture modelling of embeddings [36] provide density-based scores, while k -nearest-neighbor methods trace local support in latent layers [13]. Recent work explores how feature norms, sparsity, and subspace decompositions influence OOD behaviour. [37] analyze feature norm statistics for OOD detection, showing that norm regularization can improve robustness, while sparsity- and subspace-based methods explicitly restrict attention to informative activation dimensions [16, 17, 38]. Kernel PCA and other spectral techniques provide nonparametric density proxies in learned feature spaces [19]. These methods are often model aware in that they operate on learned representation layers, but they typically remain global in the input space and do not incorporate the task-specific importance of individual covariates. Moreover, the vast majority are tailored to discrete-label deep networks.

2.4. Graph and Time-Series OOD

Structured domains are a particularly active area of OOD research. On graphs, methods such as OOD-GNN [39], Individual and Structural Graph Information Bottlenecks (IS-GIB) [40], and causal attention mechanisms [41] improve the robustness of graph neural networks under distribution shifts by reducing reliance on spurious correlations and emphasizing invariant substructures. Data-centric and test-time approaches further enhance graph OOD detection and robustness [42, 43, 44], and several recent surveys synthesize this rapidly growing literature [8, 7]. For time series, conformal and equivariance-based methods such as CODiT [45] and related conformal time-series techniques [46, 9] provide distribution-free guarantees under temporal distortions. These structured approaches demonstrate the value of incorporating domain geometry and invariances into OOD handling, but they largely focus on graph and sequence models rather than tabular regression or survival.

2.5. Conformal and Statistical Perspectives

Conformal prediction [47] provides distribution-free, finite-sample-calibrated p -values or intervals for test inputs via non-conformity scores. Recent work has explicitly connected conformal inference and OOD detection. [48] develop integrative conformal p -values for OOD testing that leverage side information and labelled outliers, while [49] propose a multiple-testing framework that combines several model-derived statistics into a single OOD decision rule with error guarantees. [50] show how arbitrary outlier detection statistics can be wrapped in a conformal framework to produce valid p -values and finite-sample guarantees on false positive rates, while

[51] explicitly treat OOD scores as non-conformity measures and introduce conformal AUROC and FPR methods to obtain calibrated OOD decisions and more realistic evaluation of detection performance. Conformal methods have also been adapted to specialized settings such as time series [45, 46] and graphs [52]. In our work we focus on designing a model-aware, subspace-aware OOD score; such a score could in principle be integrated with conformal calibration, but we leave that extension for future work.

2.6. Positioning our Contributions

Despite substantial progress, most existing OOD detectors focus on one of two aspects: they are either model aware, operating on the trained model’s outputs or internal representations, or they are subspace aware in the sense of exploiting learned feature subspaces, but rarely both in a way that directly reflects the learned conditional $P_{Y|X}$ and the importance of individual covariates. Classification methods, including recent margin-based approaches [53, 54] and geometric techniques for graphs and time series [39, 45, 41], are typically model aware but not tailored to continuous outcomes or clinical survival analysis. Regression and survival methods are mostly uncertainty-based and operate globally on the full feature space, making no explicit distinction between perturbations in predictive versus nuisance coordinates. Even recent subspace-based approaches work with latent activation subspaces rather than subspaces defined by the predictive structure of the model.

Our framework directly addresses this gap by *embedding model awareness together with subspace relevance* into the OOD detection process. Using the fitted supervised model (here, a random forest) we construct localized, task-relevant neighborhoods that reflect both the learned mapping from X to Y and the model’s prioritization of variables. OOD scores are computed within these model-derived subspaces, without requiring global density estimation or explicit modelling of \mathbb{P}_X , and can be applied to regression, survival analysis, and other outcome types. In this sense our method targets functionally OOD inputs, those that alter $\mathbb{P}_{Y|X}$ in regions the model actually uses, rather than purely geometric outliers in the full input space.

3. Methodology

Our approach to OOD detection in supervised learning follows the principle set out above: the changes that matter are those that threaten the model’s predictive validity. An input is considered suspicious if it departs from the model’s learned relationship in a way that undermines validity. For a given input $x = (x^{(1)}, \dots, x^{(d)}) \in \mathbb{R}^d$, we therefore seek an OOD score $d(x)$, with larger values indicating greater departure from the training distribution in the model-relevant subspace.

We begin by fitting a supervised model to labeled training data $(x_1, y_1), \dots, (x_n, y_n)$. In our implementation, we use a random forest (RF) ensemble [55], which supports a wide range of outcome types, including regression, classification, and survival analysis. This flexibility is valuable because it allows the OOD framework to operate without restriction on the prediction task. The RF model also produces a rich collection of interpretable, rule-based regions that are the foundation of our method. Here a *rule* refers to a decision path of a tree (equivalently terminal node of a tree) which can be viewed a logical condition that defines a region of the input space; for example, $x^{(1)} > 3$ and $x^{(5)} < 1$, which selects a subset of the data according to feature thresholds. These regions are combined with variable-prioritized subspace analysis to quantify how atypical a test input is relative to the model’s learned structure.

Our method builds on Variable Priority (VarPro) [56, 57, 58], a framework for model-independent feature selection. Using the rule-based regions from the ensemble, VarPro assesses variable importance by comparing outcome behavior within each region to that in a corresponding *release region*, where constraints on selected variables are removed. An important strength of VarPro is its ability to identify true signal variables even in high dimensional, nonlinear, or

weak-signal settings. This capability is central to enabling subspace-focused awareness that avoids contamination from irrelevant features.

The remainder of this section details the various steps in constructing the OOD distance function. A complete summary is given in Algorithm 1, which we refer to as *outPro* (OOD using variable priority).

3.1. Frequency Profiling via Rule Relaxation

The first step in computing the OOD distance is to construct a frequency profile for each training point based on its co-occurrence with the test input x . These profiles are formed using a collection of release regions derived from the RF ensemble. Frequency profiling is restricted to the coordinates of high quality variables identified by VarPro.

We begin by extracting the set $\mathcal{R}(x)$ of decision rules, that is terminal nodes from the ensemble, which contain x . Each rule $\zeta \in \mathcal{R}(x)$ defines a hyperrectangle $R(\zeta) \subset \mathbb{R}^d$ determined by univariate split conditions. For each rule and each coordinate $s \in S$, where $S = \{s_1, \dots, s_q\} \subset \{1, \dots, d\}$ is the subset of task relevant variables identified by VarPro, we construct a release region $R(\zeta^s)$ by removing the constraint on variable s , which expands the region along the s axis while keeping all other bounds fixed.

For each training point $x_i = (x_i^{(1)}, \dots, x_i^{(d)})$, we count how often it falls inside each release region. For each $s \in S$, we increment a count $n_s(x_i)$ whenever $x_i \in R(\zeta^s)$ for some $\zeta \in \mathcal{R}(x)$. This yields the number of appearances of x_i across all release regions for each coordinate. The resulting frequency profile is a vector of relative frequencies

$$(p_{s_1}(x_i), \dots, p_{s_q}(x_i)) = \left(\frac{n_{s_1}(x_i)}{n(x_i)}, \dots, \frac{n_{s_q}(x_i)}{n(x_i)} \right),$$

where $n(x_i) = \sum_{s \in S} n_s(x_i)$ is the total number of release events in which x_i appears. If $n(x_i) = 0$, we set $p_s(x_i) = 0$ for all $s \in S$ and exclude x_i from neighborhood construction. These frequency vectors characterize how strongly each training point co-occurs with x .

As illustration, Figure 1 shows a three dimensional example of the release region mechanism for a single rule ζ containing a test point x (shown as a black point). The rule, corresponding to a terminal node from a tree, defines a green cube. Orange points represent training data, while blue and red highlight two specific training points, A and B, selected for comparison. Although A and B are equidistant from x in Euclidean distance, they differ in their proximity to x along the task relevant coordinates S (here dimensions 1, 2, and 3). Point B (red) lies close to x only along $x^{(2)}$ and $x^{(3)}$, whereas point A (blue) is close across all three relevant dimensions $x^{(1)}$, $x^{(2)}$, and $x^{(3)}$. The grey cuboids represent the release regions obtained by relaxing each coordinate constraint of the original rule. In this example the frequency counts are $(n_1(A), n_2(A), n_3(A)) = (1, 1, 1)$ and $(n_1(B), n_2(B), n_3(B)) = (0, 1, 1)$. Point A appears in all release regions, while point B does not appear in the one associated with $x^{(1)}$. Thus A has a more balanced frequency profile than B, and therefore as discussed next, is considered more similar to x .

3.2. Proximity Scoring from Frequency Dispersion

Using the frequency profiles, we now define a proximity score to rank the similarity of training points to the test input x . The idea is to assign higher scores to points that consistently co-occur with x across the release regions associated with coordinates $s \in S$. Recall that the vector $(p_{s_1}(x_i), \dots, p_{s_q}(x_i))$ encodes the relative frequency with which a training point x_i appears in each of these release regions. When x_i is well matched to x across the predictive dimensions, this vector tends to be nearly uniform, reflecting balanced co-occurrence under coordinate relaxations. This occurs because relaxing any single constraint still preserves overlap when the points are close in the subspace S . Such uniformity signals functional similarity under the model’s rule

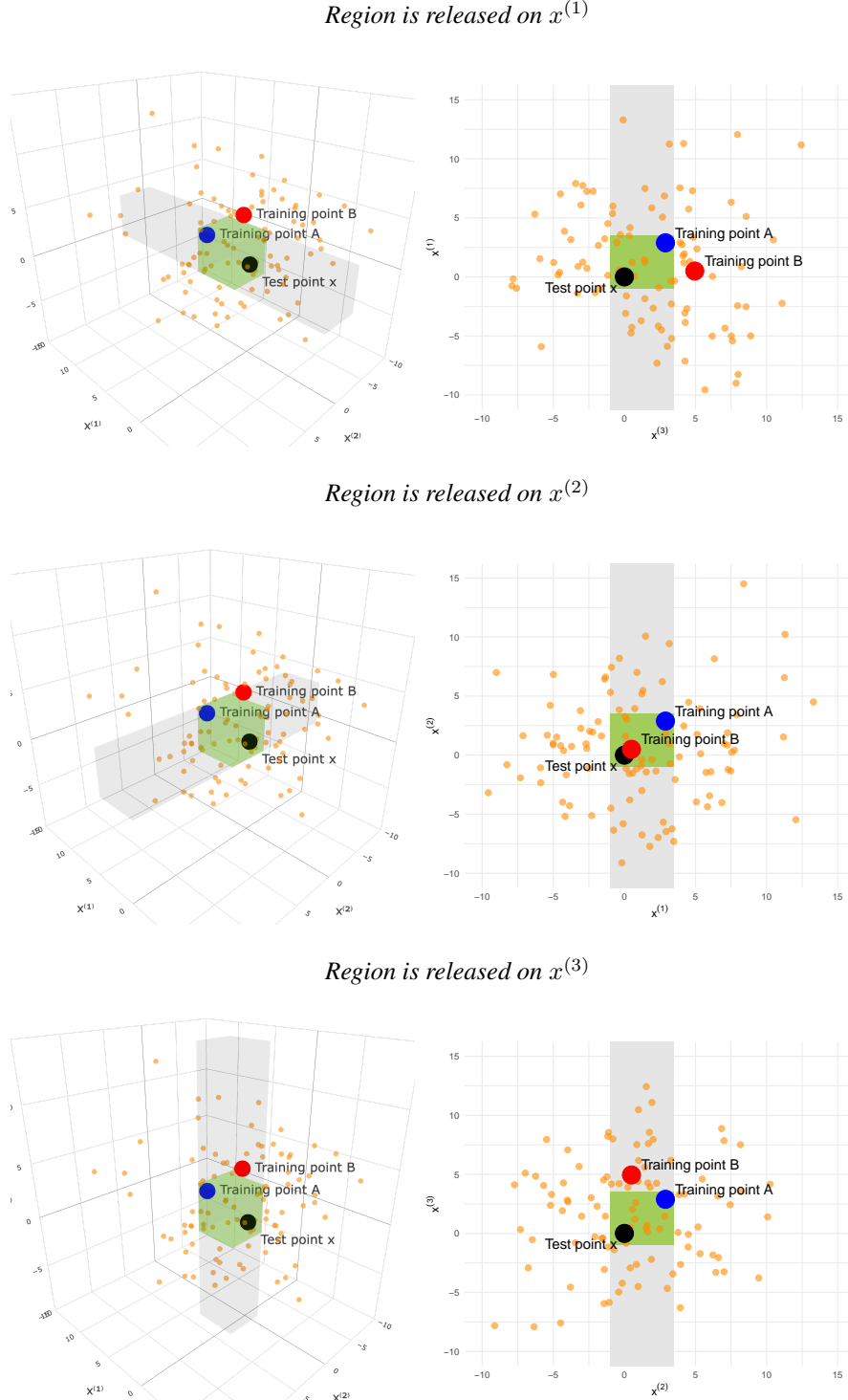


Figure 1: Illustration of the released-region mechanism used for frequency profiling. The green cube represents a rule (terminal node) containing the test point x (black), with training data shown in orange. Grey cuboids depict the three released regions formed by relaxing individual coordinate constraints. Training points A (blue) and B (red) are equidistant from x in Euclidean distance, but differ in their alignment with the task-relevant coordinates $x^{(1)}, x^{(2)}, x^{(3)}$. Point A is close to x along all three dimensions and appears in all released regions, yielding a balanced frequency profile, whereas point B is close only along $x^{(2)}$ and $x^{(3)}$, and appears in just two of the three regions.

structure. Points that are poorly matched along the predictive coordinates yield skewed or sparse profiles, indicating a weaker functional relationship.

To quantify this effect, we compute a Gini style dispersion score:

$$S(x_i) = \sum_{s \in S} p_s(x_i)(1 - p_s(x_i))$$

where higher values indicate more uniform co-occurrence. The final proximity score is defined by weighting this value by the overall frequency of appearance:

$$W(x_i) = n(x_i) \cdot S(x_i).$$

The weighting prioritizes training points that are both proximal to x and broadly represented across the ensemble.

Figure 2 provides an illustration for two hypothetical test points. When a test point relaxes a coordinate constraint, the training points that fall into the resulting release region are identified. In the figure, test point B relaxes $x^{(1)}$ and captures many nearby training points, producing larger values of $n(x_i)$ and higher weighted scores $W(x_i)$ for those neighbors. This suggests that B is well supported by the training distribution and is therefore less likely to be flagged as OOD. By comparison, test point A captures fewer training points when relaxing along $x^{(1)}$, which leads to smaller values of $n(x_i)$ and $W(x_i)$ and a higher OOD score.

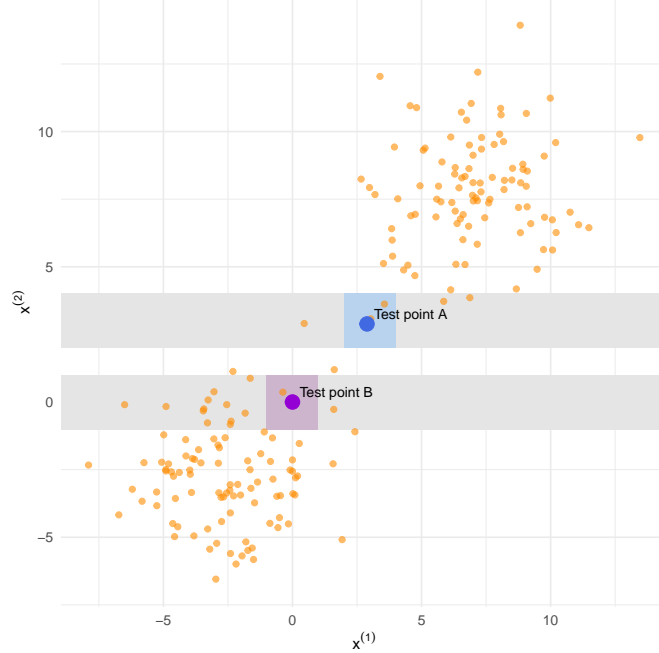


Figure 2: *Weighted proximity via dispersed co-occurrence.* For a test point, relax one coordinate at a time to form release regions and collect training points x_i that fall inside. Dispersion across coordinates is scored by $S(x_i) = \sum_{s \in S} p_s(x_i)(1 - p_s(x_i))$, and the final weight is $W(x_i) = n(x_i) S(x_i)$, where $n(x_i)$ is the total number of appearances. In the figure, B captures many neighbors when $x^{(1)}$ is relaxed, giving larger $n(x_i)$ and $W(x_i)$ and therefore a lower OOD score; A captures fewer, yielding smaller $n(x_i)$ and $W(x_i)$ and a higher OOD score.

3.3. OOD Distance via Subspace Distance Functions

Using the proximity scores $W(x_i)$, the next step is to identify a high value neighborhood for the test point x . We define $\mathcal{N}_K(x)$ as the set of K training points with the highest $W(x_i)$ values, representing the most functionally similar neighbors to x . To promote stability and reduce sensitivity to noise, we depart from traditional K nearest neighbor methods that use small K , and use instead large values (for example $K = 50$ or higher) when constructing this neighborhood.

The OOD distance for x is then obtained by measuring its separation from the neighborhood $\mathcal{N}_K(x)$ using a subspace distance function. For each neighbor $x^* \in \mathcal{N}_K(x)$ we compute a weighted distance $D(x, x^*)$ and then average the results:

$$d(x) = \frac{1}{K} \sum_{x^* \in \mathcal{N}_K(x)} D(x, x^*).$$

The subspace distance $D(x, x^*)$ uses only coordinates from S and weights those using importance scores $\{w_s\}_{s \in S}$ obtained from VarPro [56, 57]. These weights are strictly positive and normalized so that higher priority features receive stronger emphasis while weaker or irrelevant features are downweighted. Unless noted otherwise, distances are computed on standardized coordinates using training means and variances.

In the next few subsections we introduce several specific distance metrics to be used in our empirical studies.

3.3.1. Product Distance

This default metric captures joint deviation by taking the product of coordinate wise absolute differences, each raised to a power given by the importance weight w_s . Specifically,

$$D_{\text{prod}}(x, x^*) = \prod_{s \in S} \left(|x^{(s)} - x^{*(s)}| + \varepsilon \right)^{w_s},$$

where $\varepsilon > 0$ is a small constant added for numerical stability. The product penalizes small deviations across all relevant dimensions, so the distance remains low only when x and x^* are simultaneously close over the informative features.

3.3.2. OPTICS Reachability

This hybrid approach adapts the OPTICS algorithm (Ordering Points To Identify the Clustering Structure) of [59] to compute a local reachability score. Unlike global clustering methods, OPTICS builds a reachability based ordering of points using core distances and local density estimates, which provides a detailed notion of local separation without requiring a fixed number of clusters.

To compute the distance for a test input x , we apply OPTICS to $\mathcal{N}_K(x) \cup \{x\}$, where each coordinate $s \in S$ is weighted by $\sqrt{w_s}$. The OPTICS based distance is defined as the reachability of x to its nearest dense region in the high value neighborhood $\mathcal{N}_K(x)$:

$$d_{\text{optics}}(x) = \text{Reachability}(x \mid \mathcal{N}_K(x), \text{minPts}, \{w_s\}_{s \in S}),$$

where the reachability distance is obtained from the OPTICS ordering and reflects the density based separation between x and the nearest cluster core.

This approach has two main advantages: (i) it adapts to nonlinear local structures that simpler metrics may not capture, and (ii) it is computationally efficient because OPTICS is applied only to $\mathcal{N}_K(x)$ and not to the full data set. For implementation we use the `dbscan` function from the R package `optics`, with the parameter `minPts` set to 5 [60].

Algorithm 1: Variable Priority OOD Detection (outPro)

Input: Training data $\{(x_i, y_i)\}_{i=1}^n$; test point x ; number of neighbors K ; distance function $D(x, x^*)$.

Output: OOD distance score $d(x)$.

1 **Step 1: Train a supervised random forest**
 2 Fit a random forest model to $\{(x_i, y_i)\}$ and extract decision rules $\{\zeta_j\}$ for terminal nodes.

3 **Step 2: Apply VarPro to identify signal variables**
 4 Obtain the signal set $S = \{s_1, \dots, s_q\} \subset \{1, \dots, d\}$ and the importance values $\{w_s\}_{s \in S}$ using VarPro.

5 **Step 3: Identify rules containing the test point**
 6 Let $\mathcal{R}(x) = \{\zeta_j : x \in R(\zeta_j)\}$ be the set of rules whose regions contain x .

7 **Step 4: Compute relative frequencies**
 8 **for each** training point x_i **do**
 9 **for each** $s \in S$ **do**
 10 Set $n_s(x_i) = 0$.
 11 **for each** $\zeta \in \mathcal{R}(x)$ **do**
 12 Construct the release region $R(\zeta^s)$ by removing the constraint on variable s .
 13 **if** $x_i \in R(\zeta^s)$ **then**
 14 Update $n_s(x_i) \leftarrow n_s(x_i) + 1$.
 15 Compute $n(x_i) = \sum_{s \in S} n_s(x_i)$.
 16 Compute $p_s(x_i) = n_s(x_i)/n(x_i)$ for all $s \in S$.
 17 Compute $S(x_i) = \sum_{s \in S} p_s(x_i)(1 - p_s(x_i))$.
 18 Compute $W(x_i) = n(x_i) \cdot S(x_i)$.

19 **Step 5: Select the K highest scoring neighbors**
 20 Sort $\{x_i\}$ in decreasing order of $W(x_i)$ and select the top K neighbors, $\mathcal{N}_K(x)$.

21 **Step 6: Compute the OOD distance**
 22 **for each** $x^* \in \mathcal{N}_K(x)$ **do**
 23 Standardize the coordinates using training means and variances.
 24 Compute $D(x, x^*)$ using the selected distance function and the normalized importance weights $\{w_s\}_{s \in S}$.

25 Aggregate the computed distances to obtain the final OOD score $d(x)$.

3.3.3. Euclidean Distance

This standard metric computes the squared ℓ_2 distance across the task relevant coordinates, weighted by variable importance:

$$D_{\text{euclid}}(x, x^*) = \left(\sum_{s \in S} w_s \cdot (x^{(s)} - x^{*(s)})^2 \right)^{1/2}.$$

Irrelevant coordinates are excluded through subspace selection, and each remaining dimension is further weighted by its importance w_s . As a result, this metric is more robust than full space Euclidean distance in high dimensional settings.

3.3.4. Manhattan Distance

The Manhattan or ℓ_1 distance accumulates absolute differences across the task relevant coordinate:

$$D_{\text{manh}}(x, x^*) = \sum_{s \in S} w_s \cdot |x^{(s)} - x^{*(s)}|.$$

This metric is less sensitive to outliers than ℓ_2 distance and can be effective when the underlying values show sharp changes or sparsity along certain coordinates in S .

3.3.5. Mahalanobis Distance

This metric accounts for second order feature correlations in the subspace S by applying a global covariance adjustment. Let Σ_S be the empirical covariance matrix of the training data restricted to S , and let $x_S - x_S^*$ be the difference vector:

$$D_{\text{mahal}}(x, x^*) = \sqrt{(x_S - x_S^*)^\top \Sigma_S^{-1} (x_S - x_S^*)}.$$

Although this metric uses a global Σ_S estimated from the training data, it remains subspace aware through using coordinates S , benefiting from dimension reduction.

3.3.6. Minkowski Distance

This metric generalizes both Euclidean distance ($p = 2$) and Manhattan distance ($p = 1$):

$$D_{\text{mink}}(x, x^*) = \left(\sum_{s \in S} w_s \cdot |x^{(s)} - x^{*(s)}|^p \right)^{1/p},$$

where $p \geq 1$ is a user specified parameter. Larger values of p give greater weight to large coordinate deviations. In our implementation we use $p = 4$, which amplifies anomalies with strong deviations in a coordinate.

4. Comparison Methods

For baseline comparison we use a wide range of existing approaches for OOD detection. We cover the main families of detectors used in the recent literature while restricting attention to methods that (i) are applicable to continuous outcomes and standard covariate vectors, (ii) can be implemented on top of a common predictive model, and (iii) admit reliable, open-source implementations. Broadly, the comparison methods fall into four groups: (1) uncertainty-based methods that use posterior or ensemble variance as an OOD signal (Gaussian processes, deep ensembles, deep kernel learning, conformal prediction); (2) geometric and density-based methods that measure distance or density in input or latent space (Mahalanobis distance, energy score, Gaussian mixtures, deep k -nearest neighbors); (3) gradient-based methods that quantify local sensitivity of the predictor; and (4) model-based detectors tailored to our random forest engine

(outPro). Where appropriate we adapt classification-based OOD scores such as MSP, ODIN, and energy to the regression setting, and we include regression-specific methods based on predictive variance and feature-space density. Methods that require discrete class probabilities or specialized architectures (e.g., margin-based classification detectors, or graph and time-series-specific OOD methods) are discussed in Section 2 but are not used as baselines here, since they do not directly apply to our continuous-outcome benchmarks.

Unless otherwise noted, methods that rely on a neural network use the same underlying architecture implemented with the Keras API [61]. This model is a three layer feedforward network with ReLU activations, batch normalization, dropout, and a single output node trained using mean squared error loss. Predictions, gradients, and feature embeddings used for the comparison methods are all derived from this shared architecture. Methods based on Gaussian processes or random forests use separate engines as described below.

4.1. Maximum Softmax Probability (MSP)

Adapted from the classification setting [1], this version of MSP for regression computes a confidence score based on the deviation of the prediction from the mean training response:

$$\text{MSP}(x) = \frac{1}{1 + |f(x) - \bar{y}_{\text{train}}|},$$

where $f(x)$ is the predicted response. The denominator is scaled so that inputs producing predictions far from the central tendency of the training data receive smaller scores. Smaller values of $\text{MSP}(x)$ indicate potential OOD behavior.

4.2. ODIN

ODIN [10] was originally proposed for classification and uses input perturbation to amplify differences between ID and OOD inputs. In our regression adaptation, we apply a perturbation of magnitude $\epsilon = 0.01$ and then compute the MSP-style score at the perturbed input $x_{\text{perturbed}} = x + \epsilon \cdot \text{sign}(x)$:

$$\text{ODIN}(x) = \frac{1}{1 + |f(x_{\text{perturbed}}) - \bar{y}_{\text{train}}|}.$$

As in the adapted MSP, smaller values of $\text{ODIN}(x)$ indicate that the perturbed input may be OOD.

4.3. Energy Based Detection (Energy)

Following [11], we use the ℓ_2 norm of the penultimate layer feature vector evaluated at a perturbed input. In our regression setting, we apply a perturbation of magnitude $\epsilon = 0.01$ in the input direction:

$$x_{\text{perturbed}} = x + \epsilon \cdot \text{sign}(x), \quad \text{Energy}(x) = \|z(x_{\text{perturbed}})\|^2,$$

where $z(x)$ is the hidden representation from the penultimate layer of the network. Larger values of $\text{Energy}(x)$ indicate higher model confidence and are more likely to correspond to ID inputs, while smaller values suggest potential OOD status.

4.4. Mahalanobis Distance Based Detection (Mahalanobis)

We compute the Mahalanobis distance between the standardized test input and the training mean:

$$d_M(x) = \sqrt{(x - \mu)^\top \Sigma^{-1} (x - \mu)},$$

where μ and Σ are the empirical mean and covariance matrix of the training inputs. The distance is computed directly in the input space and does not use the neural network model. Larger values suggest that x may be OOD.

4.5. Conformal Prediction (CP)

Conformal prediction [47] provides model-agnostic uncertainty scores. We partition the training set into 75% for model fitting and 25% for calibration. For a new input x , let f_{calib} be the predictions on the calibration set and let $Q_{1-\alpha}$ be the $(1-\alpha)$ quantile of the absolute calibration residuals. We flag x as out of distribution if its prediction deviates from the median calibration prediction by more than this threshold:

$$\text{CP}(x) = 1 \{ |f(x) - \text{median}(f_{\text{calib}})| > Q_{1-\alpha} \}.$$

Here $\text{CP}(x) = 1$ indicates that x is considered OOD. While CP yields a binary decision at level α , the underlying nonconformity scores $|f(x) - \text{median}(f_{\text{calib}})|$ can be used to rank inputs by their degree of atypicality.

4.6. Gaussian Process Regression (GP)

We use the 1aGP package [62, 25] to fit a local approximate Gaussian process (GP) model. The GP defines a distribution over functions f such that $f(x)$ is the predicted response at test point x . The OOD score is taken to be the posterior predictive variance:

$$\text{GP}(x) = \text{Var}[f(x) \mid \text{data}],$$

which measures the model's uncertainty about its prediction. This variance remains small when x lies in regions densely populated by training data and increases when x is located in unfamiliar parts of the input space. Large values of $\text{GP}(x)$ therefore indicate that the input may be OOD.

4.7. Sensitivity Based Detection (Sensitivity)

Following [63], we compute the gradient of the model prediction with respect to the input using automatic differentiation:

$$\text{Sensitivity}(x) = \frac{1}{d} \sum_{j=1}^d \left| \frac{\partial f(x)}{\partial x^{(j)}} \right|.$$

This score measures how much the output changes in response to small changes in each input dimension. Larger values of $\text{Sensitivity}(x)$ suggest that the model's prediction is more volatile for that input, which may indicate OOD behavior.

4.8. Deep Kernel Learning (DKL)

We extract the penultimate layer features $z(x)$ from the neural network and fit a Gaussian process model using 1aGP in this reduced dimensional feature space [26]. The OOD score is the posterior predictive variance, as in the standard GP method. This approach combines deep feature extraction with GP-based uncertainty estimation.

4.9. Deep Ensembles (DE)

Deep ensembles [20] provide a widely used uncertainty-based baseline for OOD detection and calibration. We train M independent copies of the neural network architecture described above, each initialized with a different random seed and trained on the same data. For a test input x , let $f_m(x)$ denote the prediction from ensemble member m , $m = 1, \dots, M$. The OOD score is defined as the ensemble predictive variance:

$$\text{DE}(x) = \text{Var}_m \{ f_m(x) \},$$

which captures the degree of disagreement among ensemble members. This variance remains small for inputs where the model class is well-constrained by the training data and increases for extrapolative or poorly supported inputs. Large values of $\text{DE}(x)$ therefore indicate potential OOD behavior.

4.10. Gaussian Mixture Density in Latent Space (GMM)

Following [36], we model the distribution of hidden representations in the penultimate layer $z(x)$ of the neural network. To obtain a stable low-dimensional representation, we first apply PCA to $z(x)$ on the training data and retain the leading components, yielding dimension-reduced features $\tilde{z}(x)$. A Gaussian mixture model with one or two components is then fitted to $\tilde{z}(x)$ on the training set. For a test input x , we compute the mixture density $p(\tilde{z}(x))$ implied by the fitted model and define the OOD score as the negative log-density,

$$\text{GMM}(x) = -\log p(\tilde{z}(x)).$$

Inputs that fall in low-density regions of this latent feature space relative to the training data yield large $\text{GMM}(x)$ scores and are more likely to be OOD.

4.11. Deep k -Nearest Neighbors in Latent Space (DkNN)

Deep k -nearest-neighbor (DkNN) methods measure how well a test input is supported by nearby training examples in a learned latent space [13]. Using the penultimate layer features $z(x)$, we compute, for each test point x , the Euclidean distances from $z(x)$ to its k nearest neighbors among the training features. The OOD score is the average distance to these neighbors:

$$\text{DkNN}(x) = \frac{1}{k} \sum_{j=1}^k \|z(x) - z(x_{(j)})\|_2,$$

where $x_{(j)}$ are the k nearest training inputs in latent space. Larger values of $\text{DkNN}(x)$ indicate that the test point lies in a sparsely populated region of the feature space and may be OOD.

5. Benchmarking OOD Detection Methods in Regression

We evaluate performance using a combination of simulated and real regression problems. On synthetic data, we use a well known machine learning model with independent covariates (Section 5.1), which provides a shift-based anomaly framework with clearly defined ground-truth labels. For real data, we consider two sets of experiments. The first set is a large collection of regression benchmarks (Section 5.3) with different sample sizes, dimensions, and signal-to-noise ratios. The second set uses high-dimensional microarray survival studies (Section 5.4), where the number of features greatly exceeds the sample size. For the real-data experiments, anomalies are generated using a copula-based strategy described in Section 5.2, which allows targeted perturbations of marginal distributions and joint dependence. Test cases are drawn from a held-out subset of the data, and anomalous inputs are created by perturbing selected features to simulate OOD behavior.

5.1. Friedman Simulation

We first consider a simulated regression setting based on the well-known Friedman model [64]. Each covariate $X^{(j)} \sim U[0, 1]$ independently for $j = 1, \dots, d$. The response is generated according to

$$Y = 10 \sin(\pi X^{(1)} X^{(2)}) + 20(X^{(3)} - 0.5)^2 + 10X^{(4)} + 5X^{(5)} + \varepsilon,$$

where $\varepsilon \sim N(0, \sigma^2)$ and the remaining $d - 5$ covariates are irrelevant noise features. Unless otherwise noted, we use $d = 10$ and $\sigma = 1$.

To simulate OOD instances, we apply a fixed additive shift to a subset of features identified as predictive of the outcome. Although the true signal variables are known in this simulation, we use a data driven approach, tree based gradient boosting [65], to rank features by their contribution to

predictive accuracy. This mirrors the methodology to be used in our later real data experiments and ensures consistency across settings. Gradient boosting builds an ensemble of regression trees, using reductions in squared error to evaluate and rank variable importance. From the ranked list, the top ten percent of features are selected, and each is perturbed by a fixed additive amount scaled by its standard deviation, with direction randomly assigned for each test point. By explicitly targeting high importance features for perturbation, the resulting anomalies induce functional shifts that directly challenge the model’s learned response structure.

5.1.1. Ground Truth

The additive shift procedure is a common strategy used in OOD detection research, however, the labeling rule which defines a shifted point as anomalous has a subtle issue that is often overlooked: a shifted point may lie entirely within the support of the training distribution and therefore be entirely valid.

To see this, note that under the Friedman setup the covariates $X^{(j)}$ are independent and uniformly distributed on $[0, 1]$. Apply an additive shift $\delta = (\delta_1, \dots, \delta_d)$ to the covariate vector $X = (X^{(1)}, \dots, X^{(d)})$ to generate a perturbed point

$$X^* = X + \delta.$$

Due to independence and the bounded support condition, a shifted point X^* becomes anomalous only if at least one coordinate falls outside the unit interval. For coordinate j , the condition $X^{(j)} + \delta_j \in [0, 1]$ is equivalent to

$$-\delta_j \leq X^{(j)} \leq 1 - \delta_j.$$

Hence, the probability that all coordinates remain within the original hypercube is

$$\mathbb{P}(\text{all coordinates inside}) = \prod_{j=1}^d (1 - |\delta_j|)_+,$$

where $(a)_+ := \max(a, 0)$. The true fraction of shifted points that fall outside the support is therefore 1 minus this value, which for small shifts can be approximated to first order as $\sum_{j=1}^d |\delta_j|$ and therefore can be significantly bounded away from 1.

This shows that many nominally shifted points may still lie entirely within the original support and are therefore legitimate data values, particularly when shifts are small, or the dimension is moderate. To avoid this ambiguity, we adopt the rule that a point is labeled as anomalous if and only if at least one of its coordinates falls outside $[0, 1]$.

5.1.2. Evaluation Strategy

To evaluate each method, we compute its OOD score $s(x)$ for a test point x and compare it to the distribution of training scores $\{s(x_1), \dots, s(x_n)\}$. This yields an empirical null distribution representing typical ID variation. For a specified significance level α , we define the decision rule:

$$\text{Flag } x \text{ as OOD if } s(x) > \hat{F}_{\text{train}}^{-1}(1 - \alpha),$$

where $\hat{F}_{\text{train}}^{-1}$ is the empirical quantile function computed from the training scores. This provides a nonparametric threshold that controls the false positive rate at level α , assuming the training data are ID. In all examples in this paper, we use $\alpha = 0.05$.

This calibration strategy is applied to all competing methods. Each method uses its own training scores to form the empirical null, and a test point is flagged as OOD if its score exceeds the corresponding $(1 - \alpha)$ quantile. The only exception is the conformal prediction approach, which uses calibration residuals instead of direct score values. Nevertheless, all procedures are evaluated at the same significance level α , ensuring a fair comparison.

5.1.3. Experimental Settings

We generated 100 independent datasets of size $n = 2000$ from the Friedman model. Each dataset was randomly split into 80% training and 20% testing. Anomalies were created by perturbing test points using the fixed additive shift scheme described earlier: shifts were applied to the top predictive features, as ranked by gradient boosting, and scaled by the empirical standard deviation of each feature. We considered five shift magnitudes, 0.05, 0.25, 0.5, 1.0, and 2.0. Ground-truth labels were defined via the support rule described earlier: a perturbed test point was marked anomalous if and only if at least one coordinate fell outside $[0, 1]$.

5.1.4. Results

Performance was measured by the area under the precision-recall curve (AUC-PR). Boxplots in [Figure 3](#) show that outPro methods consistently achieve the highest performance for small shifts (0.05 to 0.5), where anomalies are subtle and often close to the training distribution. Among these, the product and Manhattan metrics are typically the best, with the Euclidean, Minkowski, and optics distances close behind. Among the latent-space procedures, Gaussian mixtures (GMM) and deep k -nearest neighbors (DkNN) generally outperform classical MSP/ODIN and energy scores, but still fall short of the best outPro procedures. Deep ensembles (DE) provide reasonable performance yet exhibit lower AUC-PR for small shifts, indicating that ensemble variance alone is not sufficient to reliably detect subtle, functionally OOD perturbations.

To systematically compare methods, critical difference (CD) plots [66] are given in [Figure 4](#) (significance assessed using the Nemenyi test). In the small-shift setting (0.05, 0.25, 0.5), nearly all outPro methods cluster on the left with little to no overlap with other methods, confirming their dominant performance. The product metric is the best, with the Manhattan metric close behind. Mahalanobis-based outPro performs worse, probably because uniform covariates violate the Gaussian assumptions underlying the Mahalanobis distance. Among the non-outPro methods, DkNN and GMM are generally the strongest geometric competitors, followed by GP and DKL-based procedures. Conformal prediction, MSP, ODIN, and sensitivity scores follow.

For larger shifts (1.0, 2.0), all methods improve as anomalies move farther from the training support, and performance differences narrow. GP and DKL GP models, together with DkNN and GMM, approach the outPro methods. Nevertheless, the outPro product and Manhattan metrics remain at or near the top across all shift magnitudes. This pattern underscores a key point: methods that rely primarily on global uncertainty or global geometry in the full feature space (such as deep ensembles, Gaussian processes, and latent-space density alone) can perform well when shifts are large, but struggle with small, functionally driven perturbations. On the other hand, outPro’s model-aware, subspace-aware construction can detect subtle changes that affect the learned $\mathbb{P}_{Y|X}$ while remaining close to the training distribution in the full input space.

5.2. Copula-Based Strategy for Anomaly Generation

The Friedman simulation provided a useful controlled setting for benchmarking under the assumption of independent features with bounded support. However in real data settings, marginals may be skewed or heavy tailed and variables can exhibit complex dependence. To generate realistic anomalies in such settings, we develop a copula-based approach that allows controlled perturbations to both marginal behavior and dependence. Recent work has introduced realistic OOD benchmarks for image data, such as OOD-CV-v2 [67]; our copula-based strategy provides a complementary framework for tabular and other structured datasets.

Let $X = (X^{(1)}, \dots, X^{(d)})$ be a continuous random vector with joint CDF $F(x^{(1)}, \dots, x^{(d)})$ and marginals $F_j(x^{(j)})$. By Sklar’s theorem [68], there exists a copula C such that

$$F(x^{(1)}, \dots, x^{(d)}) = C(F_1(x^{(1)}), \dots, F_d(x^{(d)})),$$

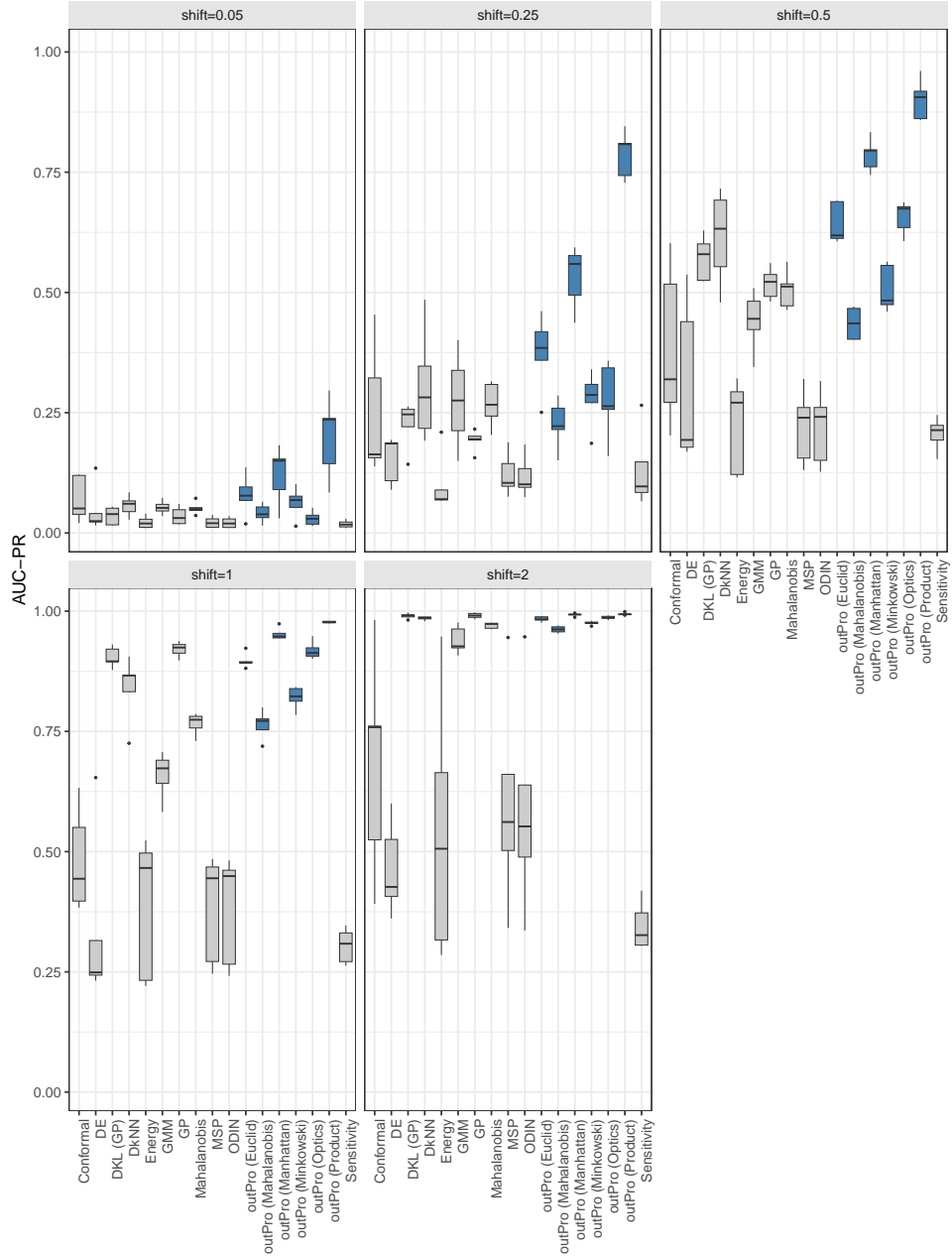


Figure 3: Boxplots of AUC-PR values for each method across 100 runs at varying shift magnitudes in the Friedman simulation. Blue indicates outPro-based methods. While performance improves for all methods as the shift magnitude increases, the outPro procedures show clear superiority for small shifts (0.05 to 0.5), where detection is most difficult.

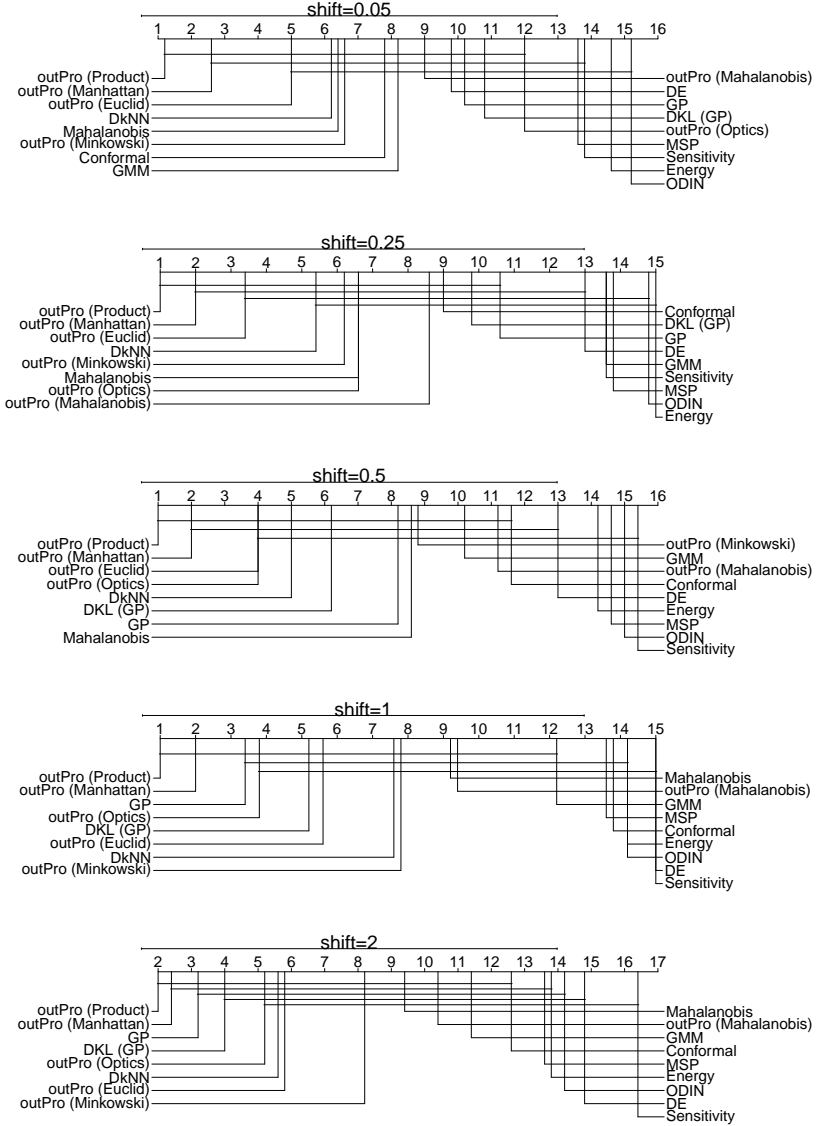


Figure 4: *Critical difference (CD) plots comparing average AUC-PR rankings for Friedman simulation for each shift magnitude. Lower ranks indicate better performance. Methods with no statistically significant difference ($\alpha = 0.05$) are connected by a horizontal bar. For small shifts (0.05, 0.25, 0.5), most outPro methods appear tightly grouped on the left, with no overlap from other methods. The product metric consistently achieves the best rank.*

where C encodes all dependence. Applying the probability integral transform to each coordinate yields

$$U^{(j)} = F_j(X^{(j)}), \quad j = 1, \dots, d,$$

so that $U = (U^{(1)}, \dots, U^{(d)})$ has uniform marginals and the joint distribution of U is C .

To synthesize anomalous data, we use the fact that any $U \in [0, 1]^d$ with uniform marginals can be mapped back to the data space via

$$X^{(j)} = F_j^{-1}(U^{(j)}),$$

thereby preserving the marginal distribution of $X^{(j)}$. We model the dependence in U with a Gaussian copula [69, 70], defined as

$$U^{(j)} = \Phi(Z^{(j)}), \quad Z \sim N(0, R),$$

where Φ is the standard normal CDF and R is a correlation matrix estimated from the training data. This formulation enables a simple strategy for controlled anomaly generation. By choosing where to apply perturbations in the copula pipeline, we can target anomalous behavior along either the dependence or marginal distributions. This pipeline is illustrated in [Figure 5](#).

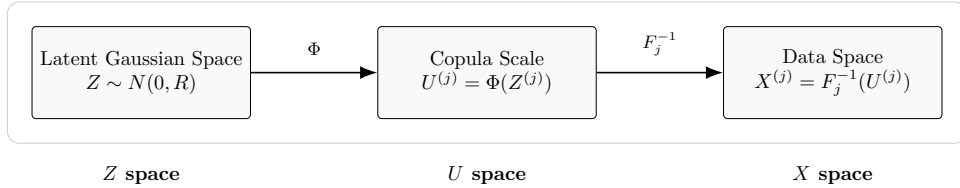


[Figure 5: Three stage transformation used by the copula anomaly generation procedure. Synthetic points are created using a latent Gaussian vector \$Z\$ \(possibly perturbed\), then mapped to the copula scale \$U\$ via the standard normal CDF \(possibly perturbed\), and finally transformed back to the data space \$X\$ using the inverse marginal CDFs \(with possible perturbations\).](#)

This strategy is used to define three anomaly modes. In the `warp` mode, U is perturbed with coordinate-wise transformations that distort the marginal shape within the observed range while leaving the copula C that encodes dependence unchanged. In the `joint` mode, the latent vector Z is perturbed to alter the dependence structure but the original marginal mapping is preserved. In the `support` mode, U is pushed toward 0 or 1, and a modified inverse CDF is applied to extrapolate beyond the observed range, moving points outside the empirical support while preserving the dependence.

Details for each of the three modes are provided below. A summary of the overall simulation procedure is given in [Algorithm 2](#).

5.2.1. `warp`: Marginal Tail Distortion

This method perturbs the marginal distributions while preserving the dependence structure encoded by a Gaussian copula. Starting with a latent vector $z = (z^{(1)}, \dots, z^{(d)})$ drawn from a multivariate normal distribution $N(0, R)$, we transform to copula coordinates using the standard normal CDF:

$$u^{(j)} = \Phi(z^{(j)}), \quad j = 1, \dots, d.$$

To induce marginal distortion, we apply a power-based warp to each coordinate:

$$u^{*(j)} = \frac{(u^{(j)})^\gamma}{(u^{(j)})^\gamma + (1 - u^{(j)})^\gamma}, \quad \gamma > 1,$$

Algorithm 2: Copula-Based Anomaly Generation and Labeling

Input: Mode $\mathcal{M} \subseteq \{\text{warp, joint, support}\}$; percentile $0 < q < 1$; training data $\{x_i\}$.

Output: $\mathcal{A} = \{(x^*, m, a^*)\}$ with anomalies x^* , mode m , label $a^* \in \{0, 1\}$.

1 Step 1: Fit copula and threshold

2 Estimate R , transform x_i to z_i via $z_i^{(j)} = \Phi^{-1}(F_j(x_i^{(j)}))$. Compute

$$d_M(x_i) = \sqrt{z_i^\top R^{-1} z_i}, \quad i = 1, \dots, n,$$

and set τ_{1-q} as the $(1 - q)$ empirical percentile of $\{d_M(x_i)\}$.

3 Step 2: Generate and label anomalies

4 Initialize $\mathcal{A} \leftarrow \emptyset$.

5 **for** $m \in \mathcal{M}$ **do**

6 **if** $m = \text{warp}$ **then**

7 Sample $z \sim N(0, R)$, set $u^{(j)} = \Phi(z^{(j)})$.

8 Apply warp:

$$u^{*(j)} = \frac{(u^{(j)})^\gamma}{(u^{(j)})^\gamma + (1 - u^{(j)})^\gamma}.$$

9 Map to data: $x^{*(j)} = F_j^{-1}(u^{*(j)})$.

10 Set $z^* = \Phi^{-1}(u^*)$.

11 Set $a^* = 1\{d_M(x^*) = \sqrt{z^{*\top} R^{-1} z^*} > \tau_{1-q}\}$.

12 **if** $m = \text{joint}$ **then**

13 Pick z_b from $\{z_i\}$, draw unit vector ζ .

14 Sample $r = \sqrt{Q}$ with $Q \sim \chi_d^2$ truncated to $[\chi_d^2(1 - q), \infty)$.

15 Set $z^* = z_b + r\zeta$.

16 Set $x^{*(j)} = F_j^{-1}(\Phi(z^{*(j)}))$.

17 Set $a^* = 1$.

18 **if** $m = \text{support}$ **then**

19 Pick z_b from $\{z_i\}$, compute $r_b = \sqrt{z_b^\top R^{-1} z_b}$.

20 Draw $r^* = \sqrt{Q^*}$ with $Q^* \sim \chi_d^2$ upper $(1 - q)$ tail.

21 Set $z^* = z_b \cdot \frac{r^*}{r_b}$.

22 Set $x^{*(j)} = \tilde{F}_j^{-1}(\Phi(z^{*(j)}))$.

23 Set $a^* = 1$.

24 Append (x^*, m, a^*) to \mathcal{A} .

25 Step 3: Return \mathcal{A} .

which concentrates mass near 0 and 1, thereby inflating the tails of the marginal distribution. The warped values are then mapped back to the data scale using the inverse empirical CDFs:

$$x^{*(j)} = F_j^{-1}(u^{*(j)}), \quad j = 1, \dots, d.$$

The resulting point x^* remains within the support of the original training data but exhibits extreme marginal values indicative of tail distortion.

To assign a ground-truth anomaly label, we return to the latent Gaussian space and compute the Mahalanobis distance of the warped point:

$$d_M(x^*) = \sqrt{z^{*\top} R^{-1} z^*},$$

where $z^* = (\Phi^{-1}(u^{*(1)}), \dots, \Phi^{-1}(u^{*(d)}))$ is the latent representation of x^* . Let τ_{1-q} denote the $(1-q)$ quantile of the empirical distribution of Mahalanobis distances computed over the training set in the latent space. The point is labeled anomalous if

$$d_M(x^*) > \tau_{1-q}.$$

In our experiments, we use $q = 0.05$ to set the anomaly threshold.

5.2.2. joint: Dependence-Based Perturbations

This strategy perturbs the joint dependence structure while retaining the original marginal mapping. Anomalies are generated by moving outward from high density regions in the latent Gaussian space toward an upper tail shell of the training distribution.

We begin by selecting a base point z_b at random from the set of latent training vectors $\{z_1, \dots, z_n\}$, where $z_i = \Phi^{-1}(F(x_i))$. A random unit direction ζ is then drawn uniformly from the unit sphere in \mathbb{R}^d . To control the degree of deviation from the training distribution, we sample a radial distance r from the upper tail of a chi-squared distribution:

$$r = \sqrt{Q}, \quad \text{where } Q \sim \chi_d^2 \text{ truncated to } [\chi_d^2(1-q), \infty),$$

with $\chi_d^2(1-q)$ denoting the $(1-q)$ quantile of a chi-squared distribution with d degrees of freedom. The perturbed latent point is then constructed as

$$z^* = z_b + r \cdot \zeta.$$

We map this point back to the data scale using the inverse copula transformation:

$$u^{*(j)} = \Phi(z^{*(j)}), \quad x^{*(j)} = F_j^{-1}(u^{*(j)}), \quad j = 1, \dots, d.$$

The resulting x^* preserves the original marginals but lies outside the typical dependence structure of the data. Each such point is treated as an anomaly and labeled accordingly.

5.2.3. support: Extrapolation Beyond Observed Range

This simulation generates anomalies by extrapolating test points beyond the support of the training distribution while using the original joint dependence structure. We begin by drawing a point z_b randomly from the latent training set $\{z_1, \dots, z_n\}$. We then compute its Mahalanobis radius:

$$r_b = \sqrt{z_b^\top R^{-1} z_b},$$

and draw a target radius r^* from the upper percentiles of a χ_d^2 distribution. The latent vector is then scaled to reach the target distance:

$$z^* = z_b \cdot \frac{r^*}{r_b}.$$

We map z^* to the copula scale using

$$u^{*(j)} = \Phi(z^{*(j)}),$$

and transform back to the data space using inverse marginals:

$$x^{*(j)} = \tilde{F}_j^{-1}(u^{*(j)}), \quad j = 1, \dots, d.$$

Here, \tilde{F}_j^{-1} denotes a modified inverse CDF that extrapolates beyond the empirical support to accommodate extreme values of $u^{*(j)}$ near 0 or 1. By design, the ground truth for x^* is set as anomalous.

5.3. Benchmarking on Diverse Real and Simulated Datasets

For benchmarking we used a curated subset of regression datasets from the Penn Machine Learning Benchmark (PMLB) repository [71, 72]. Only datasets with at least 10 features and a continuous response were used, resulting in a total of 61 datasets with dimensions ranging from $p = 10$ to 124 and sample sizes from $n = 47$ to 1066.

5.3.1. Experimental Settings

Each dataset was randomly split into 80% for training and 20% for testing. Synthetic anomalies were generated using the copula-based procedure described in Algorithm 2, with the number of anomalies matched to the number of test points. Each copula mode (warp, joint, support) was applied independently. To ensure that perturbations produced meaningful distributional shifts, we confined them to features identified as predictive of the outcome, selecting the top 10% by gradient boosting as in the Friedman simulation. As before, performance was measured by AUC-PR, with all evaluations repeated over 100 independent runs.

5.3.2. Results

Given the large number of datasets, we summarize performance by the average rank of the AUC-PR across datasets, shown as critical-difference (CD) plots in Figure 6. Under the warp simulations, the standard Mahalanobis distance score has the best average rank, followed by DkNN and outPro Mahalanobis. This ordering is expected since in the warp setting, the ground-truth notion of anomaly is defined using Mahalanobis distance, which naturally favors Mahalanobis-based scoring rules. Following the top three methods are the other outPro procedures.

The pattern shifts under the joint and support simulations. In these settings, the outPro procedures form a tight cluster on the left side of the CD plots, indicating consistently stronger performance than the baselines, with the Manhattan-based outPro achieving the best overall rank.

5.4. High-Dimensional Benchmarking

We next evaluated outPro on five high-dimensional microarray datasets commonly used in the survival analysis literature: diffuse large B-cell lymphoma (DLBCL) [73], breast cancer [74], lung cancer [75], acute myeloid leukemia (AML) [76], and mantle cell lymphoma (MCL) [77]. Each dataset contains thousands of gene expression features and right-censored survival outcomes.

To place these in a regression framework, we converted survival outcomes into continuous pseudo-responses using random survival forests (RSF) [78]. RSF models were fit to each dataset, and out-of-bag (OOB) mortality predictions were extracted for use as regression targets. Although outPro can handle survival data directly, this transformation enabled direct comparison with our previous competing regression-based methods. To improve signal-to-noise ratio, features were filtered by Cox-score ranking [79]. Table 1 summarizes sample sizes and dimensions for the filtered datasets.

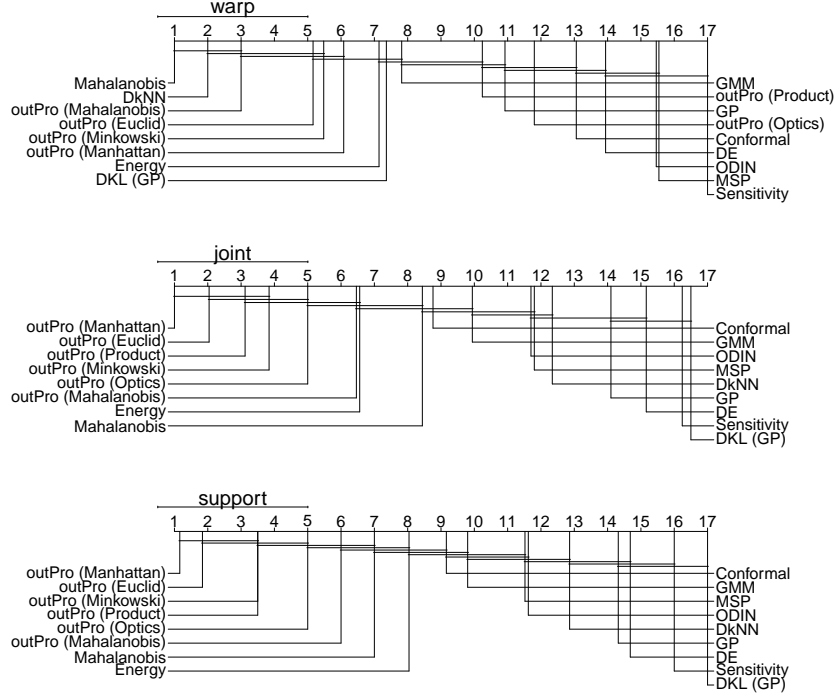


Figure 6: Critical difference (CD) plots comparing OOD detection methods across 61 PMLB regression datasets. From top to bottom, the panels correspond to three anomaly generation modes: warp, joint, and support. Methods are ranked by average AUC-PR, and statistically indistinguishable groups (at $\alpha = 0.05$) are connected by horizontal bars based on the Nemenyi test.

Table 1: Summary of high-dimensional microarray datasets used for benchmarking after Cox-score filtering.

Dataset	n	d
AML	116	629
Breast Cancer	78	475
DLBCL	240	740
Lung Cancer	86	713
MCL	92	881

5.4.1. Experimental Settings

The experimental design mirrored that of the PMLB analysis. Each dataset was split into 80% training and 20% test sets. Synthetic anomalies were generated using the copula based procedure under all three modes, with the number of anomalies matched to the number of test points. Anomaly perturbations were restricted to the top 10% of features identified as predictive by gradient boosting. Each configuration was repeated over 100 independent replicates, and performance was measured using AUC-PR.

5.4.2. Results

Boxplots of AUC-PR performance by dataset and copula mode are shown in [Figure 7](#), with an overall summary via critical difference (CD) plots given in [Figure 8](#). The qualitative picture is similar to the PMLB analysis. Across all three copula modes, the outPro procedures consistently outperform the comparison methods. Of these, Mahalanobis, Manhattan, Minkowski, and Euclidean distances are generally the best.

Among the non-outPro procedures, latent-space density and geometry methods such as the Gaussian mixture (GMM) and deep k -nearest neighbors (DkNN) scores are generally the best, particularly under the `warp` mode. The deep-kernel GP detector (DKL GP) also performs well on `warp`. On the other hand, global uncertainty and score-based methods such as deep ensembles, conformal prediction, MSP/ODIN, and the sensitivity-based score tend to lag behind, especially for the more challenging `joint` and `support` modes.

Interestingly, the product-based outPro score, which is highly competitive in the lower-dimensional PMLB benchmarks, is less dominant here, especially for the `support` mode where its AUC-PR values are typically below Manhattan, Minkowski, and Mahalanobis. One explanation is that in these high-dimensional expression datasets, many coordinates carry signal, so multiplicative combination of coordinate-wise discrepancies can amplify noise and downweight informative deviations. Additive or correlation-adjusted metrics such as the Manhattan and Mahalanobis distances are more robust here.

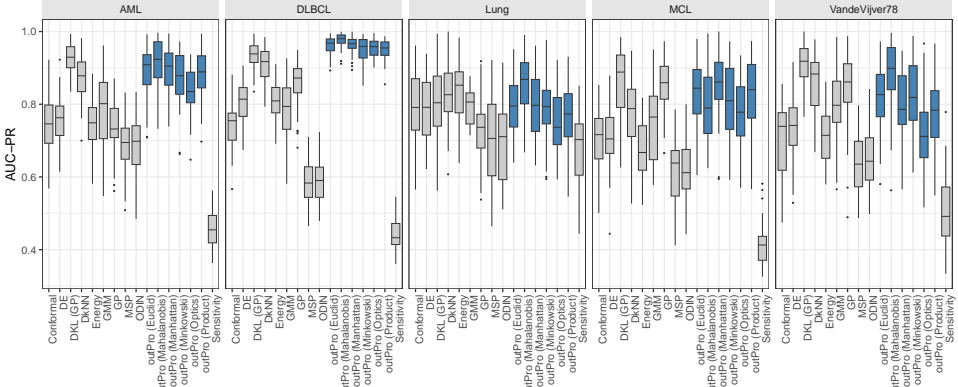
As in other high-dimensional experiments, the standard global Mahalanobis baseline could not be evaluated directly due to singular covariance matrices when $d \gg n$.

6. Evaluating Lymphadenectomy Survival Through OOD Analysis

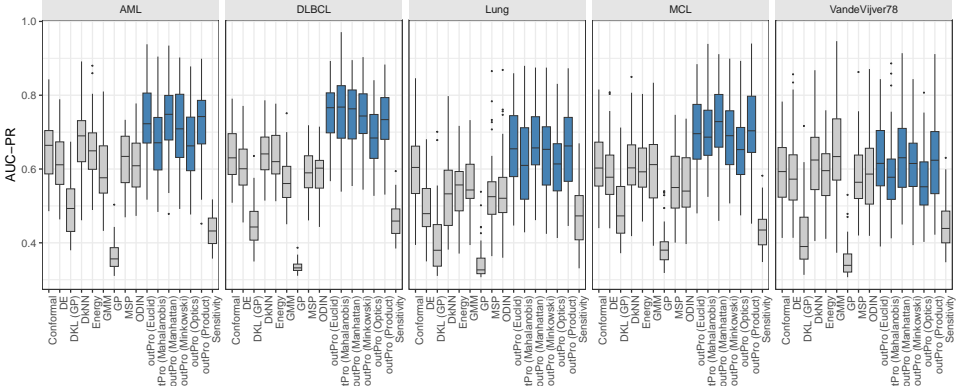
Next, we consider a case study using data from the Worldwide Esophageal Cancer Collaboration (WECC) [\[80\]](#). The registry includes patients who underwent esophagectomy alone for esophageal cancer, with follow-up on all-cause mortality available for all cases [\[81\]](#), where, as is typical in survival datasets, outcomes are right-censored for patients alive at last contact. In earlier work, this dataset was used to examine how the extent of lymphadenectomy, measured by the number of lymph nodes resected, relates to survival, with optimum values depending on tumor stage and histopathologic type. Using random survival forests (RSF) [\[78\]](#), patient-specific risk-adjusted survival curves were estimated, showing that greater lymphadenectomy was generally associated with improved five-year survival. Here, we revisit this dataset to evaluate whether patients undergoing more aggressive lymphadenectomy exhibit distinctive OOD patterns.

For the analysis, we considered $n = 6,142$ adenocarcinoma cases. Covariates included pTNM classification, number of lymph nodes resected, number of positive nodes (N), histologic grade (G), tumor location and length, residual cancer status (R), and patient demographics (age, race, gender), for a total of $d = 35$ variables. In the pTNM system, the prefix “p” indicates pathologic staging based on surgical resection specimens, and the T category describes the depth of tumor invasion, increasing in severity from pT1 through pT4.

warp



joint



support

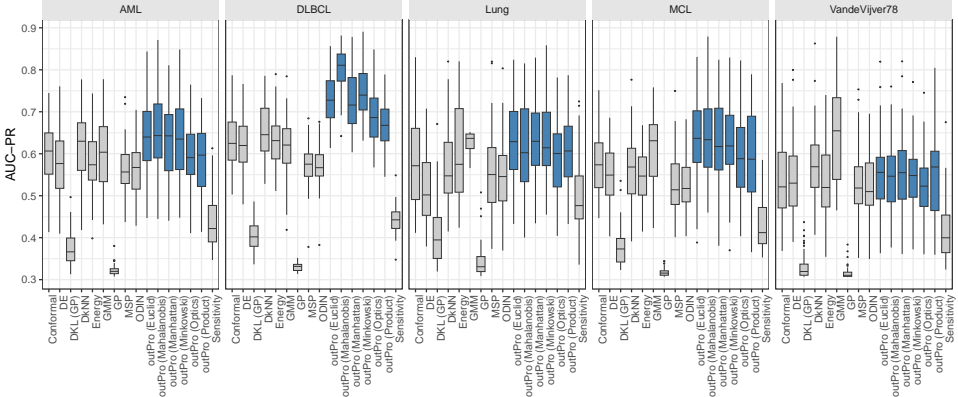


Figure 7: AUC-PR scores for each for high-dimensional microarray datasets under the three copula-based anomaly modes: *warp*, *joint*, and *support*. Each box summarizes results over 100 replications. Blue signifies *outPro* methods.

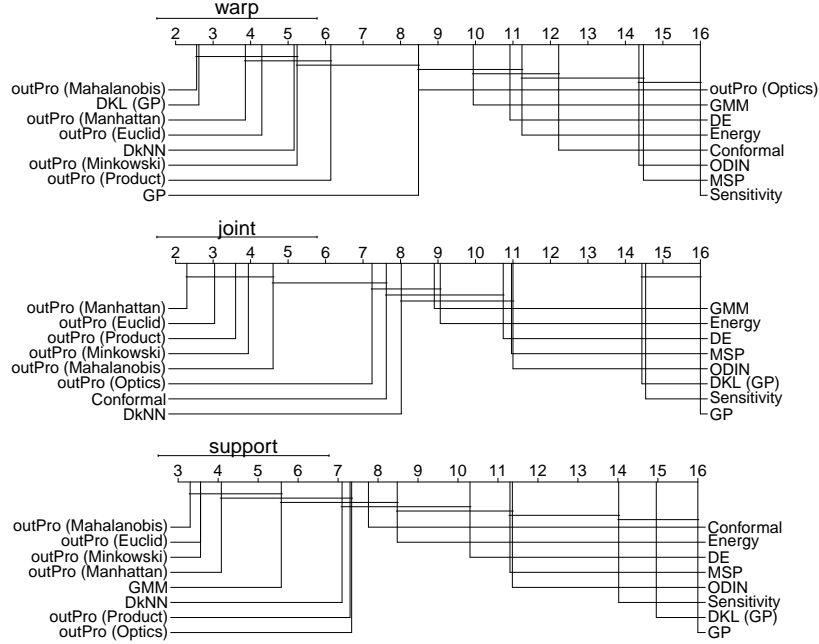


Figure 8: *Critical difference (CD) plot showing average rank performance across all for high-dimensional microarray datasets and copula modes. Lower ranks indicate better performance. All outPro methods are grouped on the left side, with the Mahalanobis and Manhattan-based approaches generally achieving the best overall rank.*

RSF was fit to the data and was subsequently used for the the predictive engine for outPro. For the OOD evaluation, we focus exclusively on patients with pT3 or pT4 tumors, combining these patients into one group. [Figure 9](#) shows the out-of-bag (OOB) five-year survival predictions from RSF for this group. The horizontal axis represents the number of lymph nodes removed during surgical lymphadenectomy, with results displayed in three panels stratified by the number of positive nodes determined from gold-standard pathology: 1–2, 3–6, and ≥ 7 . Survival generally improves with greater lymphadenectomy, although the benefit diminishes from left to right as the number of positive nodes increases.

For the OOD analysis, we systematically held out patients according to lymphadenectomy cut-off values ranging from 0 to 30 nodes, creating 31 distinct train/test scenarios. In each scenario, the test set comprised node positive pT3–4 patients with lymph node counts \geq cutoff, and all remaining patients formed the training set. A cutoff of 0 corresponds to holding out all pT3–4 patients with positive nodes. This group is highly distinct from the remaining population, as it consists entirely of individuals with deeply invasive disease and nodal involvement, and thus should (and does) produce very high OOD scores. As the cutoff increases, the held-out group becomes less extreme because it includes patients with progressively higher lymphadenectomy counts and is therefore more similar in survival to the remaining patients. For each scenario, we computed the mean OOD percentile score (0–100 scale) for the held-out group, where 100 corresponds to the most extreme OOD score under the null training distribution.

[Figure 10](#) plots the mean OOD percentile score against lymph node count, stratified by the three positive node categories. The curves decrease as the cutoff increases, reflecting that the

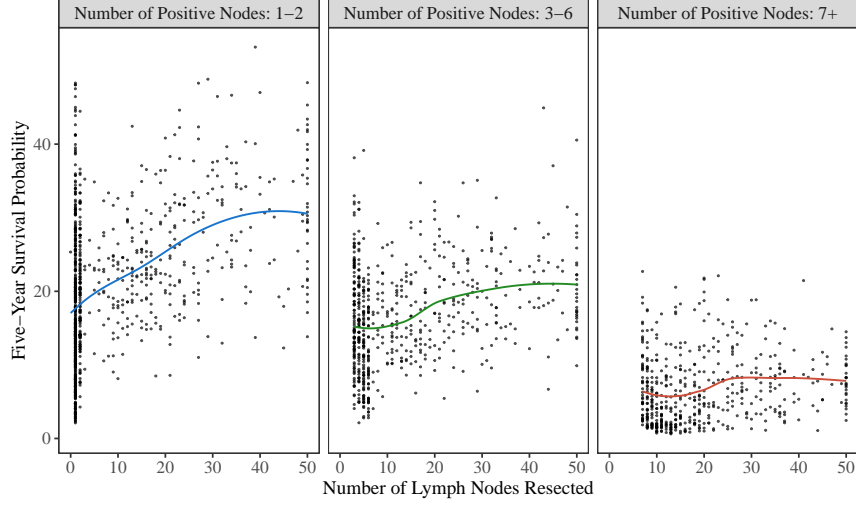


Figure 9: *Out-of-bag (OOB) five-year survival predictions from RSF for adenocarcinoma patients with pT3–4 tumors. The horizontal axis shows the number of lymph nodes removed during surgical lymphadenectomy. Results are stratified into three panels by the number of positive nodes determined from gold-standard pathology: 1–2, 3–6, and ≥ 7 . Survival generally improves with greater lymphadenectomy, although the benefit diminishes with increasing nodal involvement.*

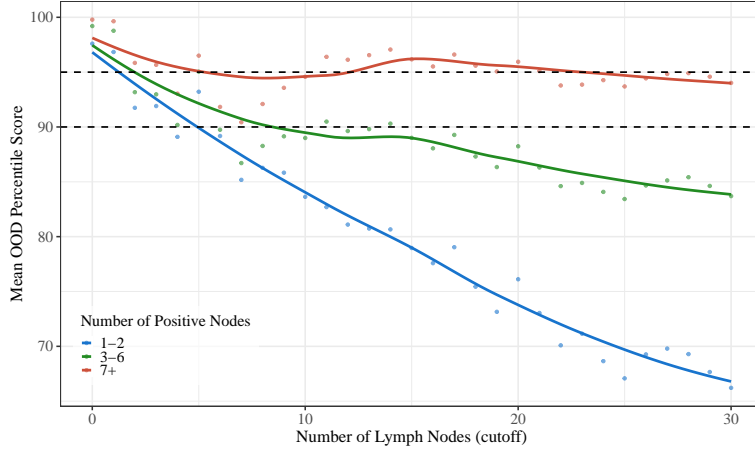


Figure 10: *Mean OOD percentile score for pT3–4 adenocarcinoma tumors as a function of lymph node count, stratified by the number of positive nodes. Scores are averaged over 31 hold-out scenarios with lymph node cutoffs from 0 to 30, where 100 represents the most extreme OOD score under the null training distribution. Curves decrease as the cutoff increases, with the steepest decline for patients with 1–2 positive nodes and the shallowest for those with ≥ 7 positive nodes.*

held-out patients become progressively less distinct. The slope of decline differs across strata in part because the plots are conditioned on the number of positive nodes; for example, in the ≥ 7 category, the lymphadenectomy count is necessarily larger than 7, which affects the range over which OOD scores can significantly drop. These patterns are also consistent with the survival trends in [Figure 9](#), where patients with heavier nodal involvement show less pronounced gains from additional lymphadenectomy. Using a vertical reference line at the 95th percentile as a threshold for safely considering a case non-OOD, the lymphadenectomy count required is approximately 3 nodes for the 1–2 and 3–6 categories, but about 30 nodes for the ≥ 7 category. Using a 90th percentile cutoff, the count increases to 5 and 10 nodes for the 1–2 and 3–6 node positive categories.

Because the surgeon does not know the true nodal status during resection, this analysis suggests that for suspected deeply invasive tumors (pT3–4), a more aggressive lymphadenectomy, say on the order of 30 nodes, is adviseable. These findings are consistent with prior WECC results, which reported optimum lymphadenectomy counts for pT3/T4 cancers ranging from 29 to 50 nodes depending on histopathologic type [\[81\]](#).

7. Summary and Limitations

We have proposed an embedded model-aware, subspace-aware framework for OOD detection that integrates variable prioritization [\[56, 57, 58\]](#) into the detection process. By constructing localized, task-relevant neighborhoods from the structure learned by the predictive model, the procedure can identify departures from the conditional distribution without relying on global distance measures or full feature density estimation. The framework is applicable across outcome types, including classification, regression, and survival analysis, and is well suited to high-dimensional settings.

Using synthetic experiments, we demonstrated that the method maintains strong detection performance under a range of anomaly mechanisms, including changes in marginal distributions and alterations to joint dependence structure. In high-dimensional microarray simulations, the method outperformed standard distance-based detectors, which often failed or became unstable due to singularity or sparsity issues.

Our case study on esophageal cancer and lymphadenectomy illustrated the clinical interpretability of OOD scores. Using pT3–4 adenocarcinoma patients from the WECC dataset, we showed that the procedure could quantify how aggressive lymphadenectomy shifts patients toward or away from anomalous behavior. The analysis suggested that for suspected deeply invasive tumors, removal of approximately 30 lymph nodes may be an appropriate surgical target when true nodal status is unknown, consistent with prior WECC findings.

In addition to strong detection performance, outPro is computationally efficient, with runtimes that remain fast across a wide range of settings. [Figure 11](#) summarizes CPU runtimes for the PMLB regression benchmarks (61 datasets) and the high-dimensional microarray studies. The horizontal axis shows sample size (n), the vertical axis shows the number of variables (d), and point size is proportional to runtime (see legend); colors distinguish the two data sources, and CPU runtimes are labeled directly on the points. Across all datasets, the maximum runtime was approximately 12 seconds. Runtimes for the high-dimensional microarray datasets were especially short, due to the effectiveness of VarPro in reducing dimensionality and the small sample sizes. Overall, the efficiency of outPro can be attributed to three features: (1) the prediction engine is based on random forests, which scale well to high-dimensional and large-sample settings; (2) priority rules are extracted from the trained ensemble using fast recursive algorithms; and (3) subspace distances are quick to compute, so neighborhood scoring adds little additional overhead.

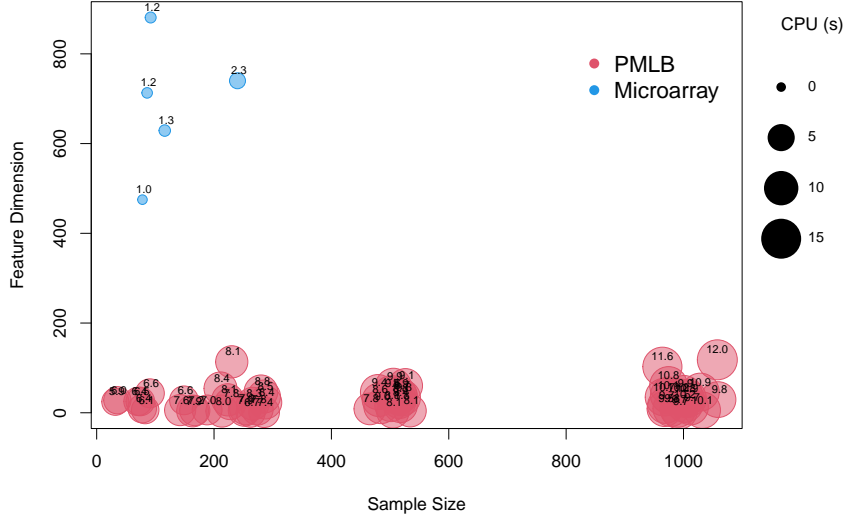


Figure 11: CPU runtimes for the PMLB regression benchmarks (61 datasets) and high-dimensional microarray studies. The horizontal axis shows sample size (n) and the vertical axis shows the number of variables (d). Point size is proportional to runtime, with the scale indicated in the legend, and times are labeled directly on each point. Colors distinguish PMLB (blue) and microarray (red) datasets. Across all settings, the maximum runtime was approximately 12 seconds.

In spite of the success of the procedure, an important question that remains is the selection of the subspace distance metric. Our experiments showed that performance can depend strongly on dimensionality. In lower-dimensional settings, the default product metric was consistently effective, while in higher-dimensional problems, metrics such as Manhattan tended to perform better. We also observed unexpectedly strong results from Mahalanobis distance in certain scenarios. These findings suggest that the choice of subspace distance warrants further theoretical analysis and systematic empirical study, particularly for high-dimensional settings.

Data and Code Availability

Our code is publicly available as an R-package `varPro` and is available at the repository <https://github.com/kogalur/varPro>. All simulated datasets can be reproduced directly from the code. Public benchmark datasets used in this study are available from the PMLB repository, and information on the microarray datasets can be found in the cited references. The esophageal cancer data from the Worldwide Esophageal Cancer Collaboration are not publicly available.

Acknowledgements

Research for the authors was supported by the National Institute Of General Medical Sciences of the National Institutes of Health, Award Number R35 GM139659 and the National Heart, Lung, and Blood Institute of the National Institutes of Health, Award Number R01 HL164405.

Conflict of Interest

The authors declare no conflicts of interest.

CRedit Authorship Contribution Statement

Min Lu: Conceptualization, Methodology, Supervision. **Hemant Ishwaran:** Conceptualization, Methodology, Writing- Original Draft, Software, Supervision, Writing - Review & Editing, Funding Acquisition.

References

- [1] Hendrycks, D. and Gimpel, K. A baseline for detecting misclassified and out-of-distribution examples in neural networks. *arXiv e-prints*, pages arXiv–1610, 2016.
- [2] Salehi, M., Mirzaei, H., Hendrycks, D., Li, Y., Rohban, M.H., and Sabokrou, M. A unified survey on anomaly, novelty, open-set, and out-of-distribution detection: Solutions and future challenges. *Transactions on Machine Learning Research*, 2022:1–81, 2022. ISSN 2835-8856. URL <https://openreview.net/forum?id=aRtjVZvbpK>. Article No. 234, published via OpenReview under CC BY 4.0.
- [3] Wu, Y., Li, T., Cheng, X., Yang, J., and Huang, X. Low-dimensional gradient helps out-of-distribution detection. *IEEE Transactions on Pattern Analysis and Machine Intelligence*, 46(12):11378–11391, 2024.
- [4] Yang, J., Zhou, K., Li, Y., and Liu, Z. Generalized out-of-distribution detection: A survey. *International Journal of Computer Vision*, 132(12):5635–5662, 2024.
- [5] Tamang, L., Bouadjenek, M.R., Dazeley, R., and Aryal, S. Handling out-of-distribution data: A survey. *IEEE Transactions on Knowledge and Data Engineering*, 2025. doi: 10.1109/TKDE.2025.3592614. Early Access.
- [6] Lu, S., Wang, Y., Sheng, L., He, L., Zheng, A., and Liang, J. Out-of-distribution detection: A task-oriented survey of recent advances. *ACM Computing Surveys*, 58(2):1–39, 2025.
- [7] Zhang, K., Liu, S., Wang, S., Shi, W., Chen, C., Li, P., Li, S., Li, J., and Ding, K. A survey of deep graph learning under distribution shifts: from graph out-of-distribution generalization to adaptation. *arXiv preprint arXiv:2410.19265*, 2024.
- [8] Li, H., Wang, X., Zhang, Z., and Zhu, W. Out-of-distribution generalization on graphs: A survey. *IEEE Transactions on Pattern Analysis and Machine Intelligence*, 2025.
- [9] Wu, X., Teng, F., Li, X., Zhang, J., Li, T., and Duan, Q. Out-of-distribution generalization in time series: A survey. *arXiv preprint arXiv:2503.13868*, 2025.
- [10] Liang, S., Li, Y., and Srikant, R. Enhancing the reliability of out-of-distribution image detection in neural networks. In *Proceedings of the 6th International Conference on Learning Representations (ICLR)*, 2018. URL <https://arxiv.org/abs/1706.02690>.
- [11] Liu, W., Wang, X., Owens, J., and Li, Y. Energy-based out-of-distribution detection. *Advances in Neural Information Processing Systems*, 33:21464–21475, 2020.
- [12] Lee, K., Lee, H., Lee, K., and Shin, J. A simple unified framework for detecting out-of-distribution samples and adversarial attacks. In *Advances in Neural Information Processing Systems 31 (NeurIPS)*, pages 7167–7177, 2018. URL <https://papers.nips.cc/paper/2018/hash/a19744e268754fb0148b017647355dd3-Abstract.html>.

- [13] Sun, Y., Ming, Y., Zhu, X., and Li, Y. Out-of-distribution detection with deep nearest neighbors. In *Proceedings of the 39th International Conference on Machine Learning*, Proceedings of Machine Learning Research, pages 20827–20840, 2022.
- [14] Ming, Y., Fan, Y., and Li, Y. POEM: Out-of-distribution detection with posterior sampling. In *Proceedings of the 39th International Conference on Machine Learning*, Proceedings of Machine Learning Research, pages 15650–15665, 2022.
- [15] Zhang, Y., Lu, J., Peng, B., Fang, Z., and Cheung, Y.m. Learning to shape in-distribution feature space for out-of-distribution detection. In *Advances in Neural Information Processing Systems*, volume 37, pages 49384–49402, 2024.
- [16] Chen, Q., Li, K., Chen, Z., Maul, T., and Yin, J. Exploring feature sparsity for out-of-distribution detection. *Scientific Reports*, 14(1):28444, 2024.
- [17] Zöngür, B., Hesse, R., and Roth, S. Activation subspaces for out-of-distribution detection. In *Proceedings of the IEEE/CVF International Conference on Computer Vision*, pages 3509–3519, 2025.
- [18] Zhu, Q. and He, Y. Out-of-distribution detection based on subspace projection of high-dimensional features output by the last convolutional layer. *arXiv preprint arXiv:2405.01662*, 2024.
- [19] Fang, K., Tao, Q., Lv, K., He, M., Huang, X., and Yang, J. Kernel PCA for out-of-distribution detection. In *Advances in Neural Information Processing Systems*, volume 37, pages 134317–134344, 2024.
- [20] Lakshminarayanan, B., Pritzel, A., and Blundell, C. Simple and scalable predictive uncertainty estimation using deep ensembles. In *Advances in Neural Information Processing Systems (NIPS)*, volume 30, 2017. URL <https://arxiv.org/abs/1612.01474>.
- [21] Gal, Y. and Ghahramani, Z. Dropout as a Bayesian approximation: Representing model uncertainty in deep learning. In *Proceedings of the 33rd International Conference on Machine Learning (ICML)*, pages 1050–1059, 2016. URL <https://arxiv.org/abs/1506.02142>.
- [22] Amini, A., Schwarting, W., Soleimany, A., and Rus, D. Deep evidential regression. In *Advances in Neural Information Processing Systems 33 (NeurIPS)*, 2020. URL <https://arxiv.org/abs/1910.02600>.
- [23] Malinin, A. and Gales, M. Predictive uncertainty estimation via prior networks. In *Advances in Neural Information Processing Systems*, volume 31, 2018.
- [24] Pequignot, Y., Alain, M., Dallaire, P., Yeganehparast, A., Germain, P., Desharnais, J., and Laviolette, F. Out-of-distribution detection for regression tasks: parameter versus predictor entropy, 2023. URL <https://arxiv.org/abs/2010.12995>.
- [25] Gramacy, R.B. laGP: Large-scale spatial modeling via local approximate Gaussian processes in R. *Journal of Statistical Software*, 72(1):1–46, 2016. doi: 10.18637/jss.v072.i01.
- [26] Wilson, A.G., Hu, Z., Salakhutdinov, R., and Xing, E.P. Deep kernel learning. In Gretton, A. and Robert, C.C., editors, *Proceedings of the 19th International Conference on Artificial Intelligence and Statistics*, volume 51 of *Proceedings of Machine Learning Research*, pages 370–378, Cadiz, Spain, 2016. PMLR. URL <https://proceedings.mlr.press/v51/wilson16.html>.
- [27] van Amersfoort, J., Smith, L., Jesson, A., Key, O., and Gal, Y. On feature collapse and deep kernel learning for single forward pass uncertainty. *arXiv preprint arXiv:2102.11409*, 2021.

[28] Marco-Valle, A., Morley, E., and Tomlin, C.J. Out of distribution detection via domain-informed Gaussian process state space models. In *Proceedings of the 2023 IEEE 62nd Conference on Decision and Control (CDC)*. IEEE, 2023.

[29] Popescu, S.G., Sharp, D.J., Cole, J.H., Kamnitsas, K., Glocker, B., et al. Distributional Gaussian processes layers for out-of-distribution detection. *Machine Learning for Biomedical Imaging*, 1(IPMI 2021 special issue):1–64, 2022.

[30] Linmans, J., Elfwing, S., van der Laak, J., and Litjens, G. Predictive uncertainty estimation for out-of-distribution detection in digital pathology. *Medical Image Analysis*, 83:102655, 2023.

[31] Shi, Y., Xu, W., and Hu, P. Out of distribution learning in bioinformatics: advancements and challenges. *Briefings in Bioinformatics*, 26(3):bbaf294, 2025.

[32] Tosaki, T., Uchino, E., Kojima, R., Mineharu, Y., Okamoto, Y., Arita, M., Miyai, N., Tamada, Y., Mikami, T., Murashita, K., et al. Out-of-distribution reject option method for dataset shift problem in early disease onset prediction. *Scientific Reports*, 15(1):19240, 2025.

[33] Azizmalayeri, M., Abu-Hanna, A., and Cina, G. Unmasking the chameleons: A benchmark for out-of-distribution detection in medical tabular data. *International Journal of Medical Informatics*, 195:105762, 2025.

[34] Zadorozhny, K., Thoral, P., Elbers, P., and Cinà, G. Out-of-distribution detection for medical applications: Guidelines for practical evaluation. In *Multimodal AI in Healthcare: A Paradigm Shift in Health Intelligence*, pages 137–153. Springer, 2022.

[35] Zamzmi, G., Venkatesh, K., Nelson, B., Prathapan, S., Yi, P., Sahiner, B., and Delfino, J.G. Out-of-distribution detection and radiological data monitoring using statistical process control. *Journal of Imaging Informatics in Medicine*, 38(2):997–1015, 2025.

[36] Pleiss, G., Souza, A., Kim, J., Li, B., and Weinberger, K.Q. Neural network out-of-distribution detection for regression tasks. 2020. URL <https://openreview.net/forum?id=ryxsUySFwr>. ICLR 2020 Submission (preprint).

[37] Park, J., Chai, J.C.L., Yoon, J., and Teoh, A.B.J. Understanding the feature norm for out-of-distribution detection. In *Proceedings of the IEEE/CVF international conference on computer vision*, pages 1557–1567, 2023.

[38] Zhang, X., Liu, Y., and Han, J. Out-of-distribution detection: Sparsification meets subspace. *Neurocomputing*, page 131240, 2025.

[39] Li, H., Wang, X., Zhang, Z., and Zhu, W. OOD-GNN: Out-of-distribution generalized graph neural network. *IEEE Transactions on Knowledge and Data Engineering*, 35(7):7328–7340, 2022.

[40] Yang, L., Zheng, J., Wang, H., Liu, Z., Huang, Z., Hong, S., Zhang, W., and Cui, B. Individual and structural graph information bottlenecks for out-of-distribution generalization. *IEEE Transactions on Knowledge and Data Engineering*, 36(2):682–693, 2024.

[41] Sui, Y., Wang, X., Wu, J., Lin, M., He, X., and Chua, T.S. Causal attention for interpretable and generalizable graph classification. In *Proceedings of the 28th ACM SIGKDD Conference on Knowledge Discovery and Data Mining*, pages 1696–1705. ACM, 2022.

[42] Guo, Y., Yang, C., Chen, Y., Liu, J., Shi, C., and Du, J. A data-centric framework to endow graph neural networks with out-of-distribution detection ability. In *Proceedings of the 29th ACM SIGKDD Conference on Knowledge Discovery and Data Mining*, pages 638–648, 2023.

- [43] Wang, L., He, D., Zhang, H., Liu, Y., Wang, W., Pan, S., Jin, D., and Chua, T.S. Goodat: Towards test-time graph out-of-distribution detection. In *Proceedings of the AAAI Conference on Artificial Intelligence*, volume 38, pages 15537–15545, 2024.
- [44] Ma, L., Sun, Y., Ding, K., Liu, Z., and Wu, F. Revisiting score propagation in graph out-of-distribution detection. In *Advances in Neural Information Processing Systems*, volume 37, pages 4341–4373, 2024.
- [45] Kaur, R., Sridhar, K., Park, S., Yang, Y., Jha, S., Roy, A., Sokolsky, O., and Lee, I. CODiT: Conformal out-of-distribution detection in time-series data for cyber-physical systems. In *Proceedings of the ACM/IEEE 14th International Conference on Cyber-Physical Systems (ICCPs 23)*. ACM, 2023. doi: 10.1145/3576841.3585931.
- [46] Nanopoulos, A. and Buza, K. Conformal prediction for out-of-distribution time-series classification. *Applied Intelligence*, 55(11):823, 2025.
- [47] Angelopoulos, A.N. and Bates, S. A gentle introduction to conformal prediction and distribution-free uncertainty quantification. *Journal of Machine Learning Research*, 22(55):1–69, 2021.
- [48] Liang, Z., Sesia, M., and Sun, W. Integrative conformal p-values for powerful out-of-distribution testing with labeled outliers. *Journal of the Royal Statistical Society: Series B*, 86(3):671–700, 2024.
- [49] Magesh, A., Wang, Y., et al. Principled out-of-distribution detection via multiple testing. *Journal of Machine Learning Research*, 24(378):1–35, 2023.
- [50] Bates, S., Candès, E., Lei, L., Romano, Y., and Sesia, M. Testing for outliers with conformal p-values. *Annals of Statistics*, 51(1):149–178, 2023.
- [51] Novello, P., Dalmau, J., and Andeol, L. Out-of-distribution detection should use conformal prediction (and vice-versa?). *arXiv preprint arXiv:2403.11532*, 2024.
- [52] Lin, X., Cao, Y., Sun, N., Zou, L., Zhou, C., Zhang, P., Zhang, S., Zhang, G., and Wu, J. Conformal graph-level out-of-distribution detection with adaptive data augmentation. In *Proceedings of the ACM on Web Conference*, pages 4755–4765, 2025.
- [53] Tamang, L., Bouadjenek, M.R., Dazeley, R., and Aryal, S. Improving out-of-distribution detection by enforcing confidence margin. *Knowledge and Information Systems*, 67:5541–5569, 2025. doi: 10.1007/s10115-025-02380-y.
- [54] Tamang, L.D., Bouadjenek, M.R., Dazeley, R., and Aryal, S. Margin-bounded confidence scores for out-of-distribution detection. In *Proceedings of the 2024 IEEE International Conference on Data Mining (ICDM)*, pages 1–10. IEEE, 2024. doi: 10.1109/ICDM59182.2024.00053.
- [55] Breiman, L. Random forests. *Machine Learning*, 45:5–32, 2001.
- [56] Lu, M. and Ishwaran, H. Model-independent variable selection via the rule-based variable priority. *arXiv*, 2409.09003, 2024. URL <https://arxiv.org/abs/2409.09003>.
- [57] Ishwaran, H. *Multivariate Statistics: Classical Foundations and Modern Machine Learning*. Chapman and Hall/CRC, Boca Raton, FL, 1st edition, 2025.
- [58] Zhou, L., Lu, M., and Ishwaran, H. Variable priority for unsupervised variable selection. *Pattern Recognition*, 172:112727, 2026. doi: 10.1016/j.patcog.2025.112727.
- [59] Ankerst, M., Breunig, M.M., Kriegel, H.P., and Sander, J. Optics: Ordering points to identify the clustering structure. In *Proceedings of the 1999 ACM SIGMOD International Conference on Management of Data*, pages 49–60. ACM Press, 1999. doi: 10.1145/304181.

304187. URL <https://doi.org/10.1145/304181.304187>.

- [60] Hahsler, M., Piekenbrock, M., and Doran, D. *dbSCAN: Fast density-based clustering with R*. *Journal of Statistical Software*, 91(1):1–30, 2019. doi: 10.18637/jss.v091.i01. URL <https://doi.org/10.18637/jss.v091.i01>.
- [61] Chollet, F. *Keras*, 2015. <https://github.com/keras-team/keras>.
- [62] Gramacy, R.B. *laGP: Local Approximate Gaussian Process Regression*, 2021. URL <https://cran.r-project.org/package=laGP>. R package version 1.5-7.
- [63] He, W., Li, X., Liang, Y., Song, L., and Li, S. Softmax response for out-of-distribution detection. In *Neural Information Processing Systems (NeurIPS) Workshop on Out-of-Distribution Generalization*, 2018. Demonstrates sensitivity (gradient) for OOD.
- [64] Friedman, J.H. Multivariate adaptive regression splines. *The Annals of Statistics*, 19(1):1–67, 1991. doi: 10.1214/aos/1176347963.
- [65] Friedman, J.H. Greedy function approximation: a gradient boosting machine. *Annals of Statistics*, 29(5):1189–1232, 2001.
- [66] Demšar, J. Statistical comparisons of classifiers over multiple data sets. *Journal of Machine Learning Research*, 7:1–30, 2006.
- [67] Zhao, B., Wang, J., Ma, W., Jesslen, A., Yang, S., Yu, S., Zendel, O., Theobalt, C., Yuille, A., and Kortylewski, A. Ood-cv-v2: An extended benchmark for robustness to out-of-distribution shifts of individual nuisances in natural images. *IEEE Transactions on Pattern Analysis and Machine Intelligence*, 2024.
- [68] Sklar, A. Random variables, joint distribution functions, and copulas. *Kybernetika*, 9(6):449–460, 1973.
- [69] Joe, H. *Dependence Modeling with Copulas*. CRC Press, 2014.
- [70] Nelsen, R.B. *An Introduction to Copulas*. Springer Series in Statistics. Springer, 2nd edition, 2006.
- [71] Olson, R.S., La Cava, W., Mustahsan, Z., Varik, G., and Moore, J.H. PMLB: A large benchmark suite for machine learning evaluation and comparison. *BioData Mining*, 10(1):36, 2017. doi: 10.1186/s13040-017-0154-4.
- [72] Palaniappan, L., Lengerich, B.J., Olson, R.S., and Moore, J.H. *pmlbr: R Interface to the Penn Machine Learning Benchmark (PMLB)*, 2020. URL <https://CRAN.R-project.org/package=pmlbr>. R package version 0.2.1.
- [73] Rosenwald, A., Wright, G., Chan, W.C., Connors, J.M., Campo, E., Fisher, R.I., Gascoyne, R.D., Muller-Hermelink, H.K., Smeland, E.B., and Staudt, L.M. The use of molecular profiling to predict survival after chemotherapy for diffuse large-b-cell lymphoma. *New England Journal of Medicine*, 346:1937–1947, 2002.
- [74] van’t Veer, L.J., Dai, H., van de Vijver, M.J., He, Y.D., Hart, A.A., Mao, M., Peterse, H.L., van der Kooy, K., Marton, M.J., Witteveen, A.T., et al. Gene expression profiling predicts clinical outcome of breast cancer. *Nature*, 415:530–536, 2002.
- [75] Beer, D.G., Kardia, S.L., Huang, C.C., Giordano, T.J., Levin, A.M., Misek, D.E., Lin, L., Chen, G., Gharib, T.G., Thomas, D.G., et al. Gene-expression profiles predict survival of patients with lung adenocarcinoma. *Nature Medicine*, 8:816–824, 2002.
- [76] Bullinger, L., Döhner, K., Bair, E., Fröhling, S., Schlenk, R.F., Tibshirani, R., Döhner, H., and Pollack, J.R. Use of gene-expression profiling to identify prognostic subclasses in adult

acute myeloid leukemia. *New England Journal of Medicine*, 350:1605–1616, 2004.

- [77] Rosenwald, A., Wright, G., Wiestner, A., Chan, W.C., Connors, J.M., Campo, E., Gasc-coyne, R.D., Grogan, T.M., Muller-Hermelink, H.K., Smeland, E.B., et al. The proliferation gene expression signature is a quantitative integrator of oncogenic events that predicts survival in mantle cell lymphoma. *Cancer Cell*, 3:185–197, 2003.
- [78] Ishwaran, H., Kogalur, U.B., Blackstone, E.H., and Lauer, M.S. Random survival forests. *The Annals of Applied Statistics*, 2(3):841–860, 2008.
- [79] Bair, E. and Tibshirani, R. Semi-supervised methods to predict patient survival from gene expression data. *PLoS Biol*, 2:511–522, 2004.
- [80] Rice, T., Rusch, V., Apperson-Hansen, C., and et al. Worldwide esophageal cancer collaboration. *Diseases of the Esophagus*, 22:1–8, 2009.
- [81] Rizk, N.P., Ishwaran, H., Rice, T.W., Chen, L.Q., Schipper, P.H., Kesler, K.A., Law, S., Lerut, T.E., Reed, C.E., Salo, J.A., Scott, W.J., Hofstetter, W.L., Watson, T.J., Allen, M.S., Rusch, V.W., and Blackstone, E.H. Optimum lymphadenectomy for esophageal cancer. *Annals of Surgery*, 251(1):46–50, 2010. doi: 10.1097/SLA.0b013e3181b2f6ee.